

# VARIANCE-REDUCED DIFFUSION SAMPLING VIA CONDITIONAL SCORE EXPECTATION IDENTITY

ALOIS DUSTON\* AND TAN BUI-THANH†

**Abstract.** We introduce and prove a **Conditional Score Expectation (CSE)** identity: an exact relation for the marginal score of affine diffusion processes that links scores across time via a conditional expectation under the forward dynamics. Motivated by this identity, we propose a CSE-based statistical estimator for the score using a Self-Normalized Importance Sampling (SNIS) procedure with prior samples and forward noise. We analyze its relationship to the standard Tweedie estimator, proving anti-correlation for Gaussian targets and establishing the same behavior for general targets in the small time-step regime. Exploiting this structure, we derive a variance-minimizing blended score estimator given by a state-time dependent convex combination of the CSE and Tweedie estimators. Numerical experiments show that this optimal-blending estimator reduces variance and improves sample quality for a fixed computational budget compared to either baseline. We further extend the framework to Bayesian inverse problems via likelihood-informed SNIS weights, and demonstrate improved reconstruction quality and sample diversity on high-dimensional image reconstruction tasks and PDE-governed inverse problems.

**1. Introduction.** Diffusion and flow models have achieved strong empirical performance across modalities by learning the *score*  $\nabla \log p_t$  along a decreasing-noise trajectory and integrating a reverse dynamics to synthesize samples [1–6]. Despite rapid progress in output realism and generation speed, a central bottleneck remains **sampling fidelity**: the ability of a sampler to faithfully resolve fine-scale geometric structure (e.g., thin manifolds) and to correctly represent separated modes with the right relative weights [1–3, 7]. In practice, these fine-scale density features are concentrated at small diffusion times, precisely where the standard mechanism for score estimation (e.g., Tweedie-type denoising estimators) becomes ill-conditioned and high-variance, often leading to over-smoothing and mode dropping in the generated samples [2, 7].

Most existing strategies for managing score estimator variance fall into two categories: architectural methods that embed inductive biases into network designs [1, 3, 8], and sampler-specific accelerations such as DDIM [9] and high-order ODE solvers [7, 10]. Our perspective is orthogonal to these directions: we improve the statistical estimator of the score field itself, pointwise in  $(y, t)$ , so that any downstream sampler or distillation scheme inherits lower variance and achieves higher sampling fidelity.

We develop a nonparametric, plug-and-play estimator based on a new *Conditional Score Expectation (CSE)* identity that relates scores across time through the forward semigroup. We pair this CSE estimator with the classical Tweedie estimator and show that their Monte Carlo errors are oppositely aligned—*exactly* for linear-Gaussian priors and *in expectation* under general regularity conditions on  $p_0$  for small diffusion times. This anti-alignment of the two estimators’ Monte Carlo errors lets us form a data dependent convex combination whose weight is chosen to maximize error cancellation between the constituent estimators. The resulting variance minimized score estimate can be plugged into standard reverse SDE/ODE solvers or consistency distillation, improving sampling quality without changing the model architecture or the sampler.

We also show that Bayesian inverse problems can be handled by a likelihood tilt

---

\*Oden Institute for Computational Engineering and Sciences, The University of Texas at Austin (alois.duston@utexas.edu).

†Oden Institute for Computational Engineering and Sciences, The University of Texas at Austin (tanbui@oden.utexas.edu).

of the SNIS weights, converting prior estimators to posterior ones with no change to the integrator.

Our main contributions are as follows:

- We introduce the **CSE identity**, a conditional-expectation relation for score evolution that holds exactly for all affine diffusion processes—including Ornstein–Uhlenbeck, variance-preserving, and variance-exploding SDEs, thereby supplying a direct, data-driven estimator.
- We provide a **plug-in estimator for DSM**, a sampler-agnostic **blended score estimator** based on combination of classical tweedie score estimator and CSE score estimator. We show this new combined(blended) estimator reduces variance and improves sampling fidelity when used with standard reverse integrators.
- We adapt our **blended score estimator** to **Bayesian inverse problems** by combining standard *likelihood-tilting* of SNIS weights with an additive  $\nabla_y \log p(x | y)$  likelihood-gradient term, and demonstrate improved posterior sampling performance across inverse-problem benchmarks.

**2. Relation to Prior Work.** Diffusion and score-based generative models have become a dominant approach to high-quality sampling by learning noise conditional scores and reversing a corruption process. Denoising diffusion probabilistic models (DDPM) introduced the modern denoising formulation [11], while the SDE view unified score-based diffusion with reverse time dynamics and predictor corrector samplers [2]. Subsequent architectural and training improvements further cemented performance and scalability [3, 8].

Building on this foundation, a major line of work focuses on reducing the number of function evaluations by accelerating integration or imposing consistency across noise levels. Training-free or post-hoc acceleration includes Denoising Diffusion *Implicit* Models (DDIM) [9] and high-order ODE solvers such as the Diffusion Probabilistic Model Solver (DPM-Solver) [10]. Alternative training paradigms learn vector fields directly via Flow Matching [4] or Rectified Flow [12], and Consistency Models impose algebraic relations across noise levels to enable one- or few-step generation [6]. *Our approach is complementary and orthogonal*: rather than proposing a new solver, nor a heuristic consistency constraint, we improve the *statistical estimator of the score field itself* at a fixed  $(y, t)$ . This estimator drops into any standard reverse Stochastic Differential Equation (SDE) or Ordinary Differential Equation (ODE) integrator or consistency/distillation pipeline and, by provably lowering pointwise variance through optimal blending, can improve sample quality for a fixed simulation budget.

Another active direction of research seeks improvements not from SDE solvers but from the structure of the governing equations, using the score’s Fokker–Planck equation as a source of regularization or supervision. Several works leverage the score Fokker–Planck (FP) equation to regularize denoising score matching (e.g., FP-Diffusion) [13], and Score-PINNs minimize the residual of the score PDE directly [14]. Mean-field/control formulations similarly connect sampling to forward PDEs [15]. In contrast, we work *semigroup-first*: for affine diffusion processes we derive *exact finite-time identities* that yield well-conditioned supervision at small times, and we make *variance* a first-class quantity by proving (linear–Gaussian) or motivating (single-basin) anti-alignment of Monte Carlo errors. Empirically, when the same reverse integrator is used, our variance-minimizing blend attains higher sample quality because the local score estimates have lower risk at the points where they are consumed.

Separate from score PDE theory, Nonparametric score estimation has deep connections to Reproducing Kernel Hilbert Space (RKHS) methods, including kernel exponential families and kernelized score matching. [16–20] Kernelized samplers such as Stein Variational Gradient Descent (SVGD) and Kernel Stein Discrepancy (KSD) or Maximum Mean Discrepancy (MMD) flows transport particles using functionals of the *target* score or discrepancy. [21–25] In this work, we do not use kernels to fit a parametric density, score or transport map, nor do we assume access to the exact *time-marginal* score  $\nabla \log p_t$ . Instead, we construct *kernel-weighted, nonparametric* estimators of the time-marginal score that are PDE-exact for any affine forward diffusion processes (via Tweedie and CSE) and then combine them by variance-optimal blending. The benefit is statistical—lower risk at the query  $(y, t)$ —and thus portable across samplers.

Finally, these score-based tools have increasingly been deployed beyond unconditional generation, serving as priors for posterior inference in imaging and scientific inverse problems [26–28]. Our framework contributes a variance-aware, semigroup-grounded *estimator* that, via a simple likelihood tilt of SNIS weights, converts prior estimators into posterior ones without altering the reverse integrator. This keeps the efficiency gains of the blended score estimator  $\hat{s}_{\text{BLEND}}$  (3.17) while changing only the weighting.

### 3. Theory: From Exact Identities to Optimal Estimators.

**3.1. Score-Based Sampling with the Ornstein–Uhlenbeck Process.** In the following, we use the typical notation in that random variables are denoted by capital letters, while lowercase letters are for their values.

Score-based generative models first define a “forward process” that corrupts data with noise over a pseudo-time variable  $t$ . We focus on the Ornstein–Uhlenbeck (OU) process as a canonical worked example (it admits closed-form transitions); the key identities and estimator formulas used below extend to general (time-inhomogeneous) affine diffusions, with the corresponding derivations collected in Appendix A. The Ornstein–Uhlenbeck (OU) process is defined by the following Stochastic Differential Equation (SDE):

$$(3.1) \quad dX_t = -X_t dt + \sqrt{2} dW_t, \quad X_0 \sim p_0,$$

where  $X_0 := X_{t=0}$  is distributed according to the data distribution  $p_0$ . The OU SDE in (3.1) has the closed-form forward update

$$x_t = e^{-t} x_0 + \sqrt{1 - e^{-2t}} \varepsilon, \quad \varepsilon \sim \mathcal{N}(0, I).$$

We denote the (Gaussian) transition kernel by

$$(3.2) \quad p_{t|0}(x_t | x_0) = \mathcal{N}(x_t; e^{-t} x_0, (1 - e^{-2t}) I).$$

The time- $t$  marginal is then given by the convolution

$$(3.3) \quad p_t(x_t) = \int p_{t|0}(x_t | x_0) p_0(x_0) dx_0.$$

We define the time- $t$  **score function** by

$$(3.4) \quad s(x, t) := \nabla_x \log p_t(x).$$

The corresponding **OU posterior** of the earlier state  $x$  given the latter state  $y$  is

$$(3.5) \quad p_{t|0}(x | y) = \frac{p_0(x) p_{t|0}(y | x)}{p_t(y)}.$$

In particular, for any test function  $f$  we have  $\mathbb{E}[f(X_0) | X_t=y] = \int f(x) p_{t|0}(x | y) dx$ . We will use the shorthand “ $p_{t|0}(x_0 | y)$ ” throughout to denote the OU posterior (also listed in the notation table).

As  $t$  increases, the distribution of  $X_t$ , denoted by  $p_t(x)$ , smoothly approaches a standard normal distribution. The generative task is to reverse this process. This is possible by solving the corresponding time-reversal SDE:

$$dX_t = [X_t + 2s(X_t, t)]dt + \sqrt{2}d\bar{W}_t,$$

where  $dt$  is a positive time step for the backward process. If we can accurately estimate the score function  $s(\cdot, t)$ , we can reverse the diffusion to generate new data. This is the premise of all Denoising Score Matching (DSM) generative models.

**3.2. The Tweedie Identity and Denoising Score Matching.** A foundational result, Tweedie’s formula [29, 30], provides an exact expression for the OU score function in terms of a conditional expectation over the initial data:

$$s(y, t) = -\frac{1}{1 - e^{-2t}} \mathbb{E}_{x_0 \sim p_{t|0}(\cdot | y)} [y - e^{-t}x_0],$$

where the conditional expectation is taken with respect to the OU posterior  $p_{t|0}(x_0 | y)$  defined in (3.5). Equivalently, if  $p_0$  denotes the data distribution at time 0, the OU forward transition admits the Gaussian kernel

$$(3.6) \quad K_t(y | x_0) := p_{t|0}(y | x_0) = \mathcal{N}(y; e^{-t}x_0, (1 - e^{-2t})I) \propto \exp\left(-\frac{\|y - e^{-t}x_0\|^2}{2(1 - e^{-2t})}\right).$$

Given a reference set of particles  $\{x_0^i\}_{i=1}^{N_{\text{ref}}} \sim p_0$ , we can form a nonparametric Tweedie estimator for the score using self-normalized importance sampling (SNIS) [31, 32], as follows

$$(3.7) \quad \hat{s}_{\text{TWD}}(y, t) = -\frac{1}{1 - e^{-2t}} \sum_{i=1}^{N_{\text{ref}}} \tilde{w}_i(y, t) (y - e^{-t}x_0^i),$$

where the (unnormalized) importance weights are defined by evaluating the OU transition kernel at the reference particles,

$$(3.8) \quad w_i(y, t) := K_t(y | x_0^i), \quad \tilde{w}_i(y, t) := \frac{w_i(y, t)}{\sum_{j=1}^{N_{\text{ref}}} w_j(y, t)}.$$

For the remainder of the paper, any importance weights denoted  $w_i$  (and their normalized versions  $\tilde{w}_i$ ) refer to the OU transition weights (3.8) unless explicitly stated otherwise.

**3.3. The CSE Identity.** Most existing diffusion models rely purely Tweedies identity to define their score matching loss and often overlook the underlying dynamics of the score function itself. Our work is founded on an exact analytical solution that describes its finite-time evolution, which we introduce in the following lemma (the proof for a general case is presented in [section A](#)).

LEMMA 3.1 (Conditional Score Expectation (CSE)). *Let  $p_0$  be a distribution on  $\mathbb{R}^d$ , let  $p_{t|0}(\cdot | y)$  denote the OU posterior defined in (3.5), and let  $s(\cdot, t)$  denote the time- $t$  score function defined in (3.4). Then, for any  $t > 0$ ,*

$$(3.9) \quad s(y, t) = e^t \mathbb{E}_{x \sim p_{t|0}(\cdot | y)}[s_0(x)].$$

*Proof (OU case).* Let  $K_t(y | x) := p_{t|0}(y | x)$  denote the OU transition kernel in (3.2). Differentiating the Gaussian density gives the cross-derivative identity

$$\nabla_y K_t(y | x) = -e^t \nabla_x K_t(y | x).$$

Using  $p_t(y) = \int K_t(y | x)p_0(x) dx$  and differentiating under the integral sign,

$$\nabla_y p_t(y) = \int \nabla_y K_t(y | x)p_0(x) dx = -e^t \int \nabla_x K_t(y | x)p_0(x) dx.$$

Assuming boundary terms vanish, integration by parts yields

$$\int \nabla_x K_t(y | x)p_0(x) dx = - \int K_t(y | x) \nabla_x p_0(x) dx = - \int K_t(y | x)p_0(x)s_0(x) dx.$$

Substituting back and dividing by  $p_t(y)$  gives

$$s(y, t) = \frac{\nabla_y p_t(y)}{p_t(y)} = e^t \mathbb{E}_{x \sim p_{t|0}(\cdot | y)}[s_0(x)],$$

as claimed.  $\square$

The proof above uses only the explicit OU kernel. A complementary derivation via the gradient-semigroup commutation (GSC) identity [33], together with generalizations to linear/affine SDEs, is given in Appendix A. This identity provides a constructive procedure for score estimation. Given a set of reference particles at initial time  $\{x_0^i, s_0(x_0^i)\}_{i=1}^{N_{\text{ref}}}$ , we can form a corresponding non-parametric **CSE estimator** by replacing the conditional expectation with a self-normalized importance sampling (SNIS) average:

$$(3.10) \quad \hat{s}_{\text{CSE}}(y, t) = e^t \sum_{i=1}^{N_{\text{ref}}} \tilde{w}_i(y, t) s_0(x_0^i).$$

This CSE estimator for  $s(y, t)$  applies when the initial score  $s_0(x) = \nabla_x \log p_0(x)$  is either known analytically or can be well-approximated, and is sufficiently regular such that the estimator variance is controlled. This setting describes many problems in scientific computing. For instance, in molecular dynamics,  $s_0$  can be computed from a known potential function [34, 35], and in PDE-constrained inverse problems, it can be computed using adjoint methods [36–44]. However, existing diffusion-based approaches to these problems have generally not leveraged this readily available information.

**3.4. Optimal Blending of Complementary Estimators.** The Tweedie estimator (3.7) and the CSE estimator (3.10) converge to the same true score but have two important complementary finite-sample properties. In particular, subsection 3.4.1 discusses their opposite variance growth and decay with pseudo time  $t$ , and subsection 3.4.2 shows that their finite sample errors are negatively correlated. In subsection 3.4.3, we exploit the negative correlation in their sample errors to provide a variance-minimal optimal convex blending of the two estimators.

**3.4.1. Opposite growth and decay of the two estimators.** The Monte Carlo variances of the CSE (3.10) and Tweedie (3.7) score estimators scale in opposite directions with diffusion time  $t$ : CSE is best conditioned at small  $t$ , while Tweedie is best conditioned at large  $t$ . From (3.7) and (3.10) we obtain the variance scalings

$$(3.11) \quad \text{Var}[\hat{s}_{\text{CSE}}] \propto \frac{e^{2t}}{N_{\text{ref}}}, \quad \text{Var}[\hat{s}_{\text{TWD}}] \propto \frac{e^{-2t}}{N_{\text{ref}}(1 - e^{-2t})^2}.$$

These rates directly imply complementary time-regime behavior. As  $t \rightarrow 0$ , we have  $1 - e^{-2t} \sim 2t$ , so

$$\text{Var}[\hat{s}_{\text{TWD}}] \propto \frac{e^{-2t}}{N_{\text{ref}}(1 - e^{-2t})^2} \sim \frac{1}{4N_{\text{ref}} t^2},$$

which diverges, whereas  $\text{Var}[\hat{s}_{\text{CSE}}] \propto e^{2t}/N_{\text{ref}} \rightarrow 1/N_{\text{ref}}$  remains bounded. Conversely, as  $t$  increases,  $\text{Var}[\hat{s}_{\text{CSE}}]$  grows like  $e^{2t}$ , while  $\text{Var}[\hat{s}_{\text{TWD}}]$  decays like  $e^{-2t}$  (since  $1 - e^{-2t} \rightarrow 1$ ), yielding a stable large- $t$  Tweedie estimate.

**3.4.2. Negative correlation of the two estimators.** Beyond their opposite variance scaling in  $t$  (subsection 3.4.1), the CSE and Tweedie estimators also exhibit *negatively aligned* Monte Carlo errors. We now formalize this phenomenon. In the *linear-Gaussian* case, the anti-correlation is *exact* and purely algebraic. Supplementary empirical diagnostics for this phenomenon—correlation curves across time and the time-dependent variance/bias behavior of the two estimators—are deferred to subsection E.1.

**PROPOSITION 3.2** (Gaussian case: exact anti-correlation). *Assume that  $p_0 = \mathcal{N}(\mu_0, \Sigma)$  with  $\Sigma \succ 0$ . For a given  $(y, t)$ , let*

$$\hat{\mu}_{\text{SNIS}} := \sum_{i=1}^{N_{\text{ref}}} \tilde{w}_i x_0^i, \quad \mu := \mathbb{E}_{p_0}[\hat{\mu}_{\text{SNIS}}], \quad \Delta := \hat{\mu}_{\text{SNIS}} - \mu.$$

Let  $\hat{s}_{\text{CSE}}(y, t)$  and  $\hat{s}_{\text{TWD}}(y, t)$  be the nonparametric CSE and Tweedie estimators, and let  $s(y, t)$  denote the true time- $t$  score. Their errors

$$\varepsilon_C := \hat{s}_{\text{CSE}} - \mathbb{E}_{p_0}[\hat{s}_{\text{CSE}}] = -e^t \Sigma^{-1} \Delta, \quad \varepsilon_T := \hat{s}_{\text{TWD}} - \mathbb{E}_{p_0}[\hat{s}_{\text{TWD}}] = \frac{e^{-t}}{1 - e^{-2t}} \Delta.$$

and hence the trace of their covariance  $\text{Tr}[\text{Cov}(\varepsilon_C, \varepsilon_T)]$  is given by

$$(3.12) \quad \text{Tr}[\text{Cov}_{p_0}(\varepsilon_C, \varepsilon_T)] = \mathbb{E}_{p_0}[\varepsilon_T^\top \varepsilon_C] = -\frac{1}{1 - e^{-2t}} \mathbb{E}_{p_0}[\Delta^\top \Sigma^{-1} \Delta] \leq 0.$$

with equality iff  $\Delta = 0$ .

*Proof.* The proof is straightforward: see subsection B.2 for the details.  $\square$

**Remark 3.3.** The scalar correlation (3.12) provides a theoretical justification explaining why the optimal blending reduces the variances, as it appears as a key component in the variances of the blend (see Proposition 3.5). We further note that we have used the means  $\mathbb{E}_{p_0}[\hat{s}_{\text{CSE}}]$  and  $\mathbb{E}_{p_0}[\hat{s}_{\text{TWD}}]$  to compute the deviations  $\varepsilon_C$  and  $\varepsilon_T$  both CSE and Tweedie and show that the deviations are anti-correlated. We can replace SNIS mean with the exact mean  $\mu = \mathbb{E}[X_0 | X_t = y]$ , and Proposition 3.2 still holds. In this case, the result says that errors in CSE and Tweedie estimators are

anti-correlated. For sufficient large sample size  $N_{\text{ref}}$ , the biases (due to SNIS) in both CSE and Tweedie estimators are small (see also [Theorem 3.6](#)), using the exact mean (the exact score, respectively) or SNIS mean (SNIS score mean, respectively) are thus the same.

It is not obvious if the negative correlation result in [Proposition 3.2](#) can be extended to a general distribution  $p_0$ . Fortunately, for small time which is the most important period for sampling, the result still holds, under some regularity conditions for  $p_0$ , as shown in [Theorem 3.4](#).

**THEOREM 3.4** (Negative correlation for small time  $t$  and large  $N_{\text{ref}}$ ). *Suppose the operator norm of the Hessian and the third-order derivative tensor of  $\log p_0(x)$ , the derivative of the score of  $p_0$ , is bounded as follows:*

$$m(y) I \preceq -\nabla_x^2[\log p_0(x)], \quad \|\nabla_x^3[\log p_0(x)]\|_{\text{op}} \leq c < \infty, \quad \forall x \in \text{supp}(p_{t|0}),$$

where  $\|\cdot\|_{\text{op}}$  is the corresponding operator norm. Assume that  $\Sigma_{\text{eff}}^{-1} = -\nabla^2 \log p_0(\mu) \succeq 0$  and that the important weights are uniformly bounded as  $0 < w_{\min} \leq w_i \leq w_{\max}$ . Then there exists  $N_{\text{ref}}^*$  and  $t^*$  such that

$$\mathbb{E}_{p_0}[\varepsilon_T^\top(y, t) \varepsilon_C(y, t)] < 0, \quad N_{\text{ref}} \geq N_{\text{ref}}^* \text{ and } t \leq t^*.$$

*Proof.* From [\(B.2\)](#) together with [Lemma B.2](#) and [Lemma B.3](#), we need to find  $\bar{t}$  such that

$$\frac{w_{\max}}{N_{\text{ref}}} \frac{cd^{3/2}}{\kappa^{3/2}} < \text{Tr}(\Sigma_{\text{eff}}^{-1} \text{Cov}_{p_0}(\hat{\mu})).$$

From the definition of  $\kappa$  (see [Lemma B.1](#)), it is obvious that

$$\kappa \approx \frac{1}{2t},$$

and thus

$$\sqrt{\bar{t}^3} = \frac{N_{\text{ref}}}{\sqrt{8}} \frac{\text{Tr}(\Sigma_{\text{eff}}^{-1} \text{Cov}_{p_0}(\hat{\mu}))}{w_{\max} c \sqrt{d^3}},$$

and if we use the lower bound in [Lemma B.2](#), we need to find  $\bar{t}$  such that

$$\frac{w_{\max}}{N_{\text{ref}}} \frac{cd^{3/2}}{\kappa^{3/2}} < \frac{w_{\min}}{N_{\text{ref}}} \lambda_{\min}(\Sigma_{\text{eff}}^{-1}) \|\Sigma\|_{\text{op}},$$

and thus we can eliminate  $N_{\text{ref}}$  entirely in the expression of  $\bar{t}$  as

$$\sqrt{\bar{t}^3} = \frac{1}{\sqrt{8}} \frac{w_{\min}}{w_{\max}} \frac{\lambda_{\min}(\Sigma_{\text{eff}}^{-1}) \|\Sigma\|_{\text{op}}}{c \sqrt{d^3}}.$$

The proof ends by taking

$$t^* = \min \left\{ \frac{1}{2} \log \left( 1 - \frac{1}{m(y)} \right), \bar{t} \right\}.$$

□

**3.4.3. Optimal blending as variance minimization.** Given the complementary growth/decay of the variance profiles and, more importantly, the negative correlation between the CSE (3.10) and Tweedie (3.7) estimators, we consider a linear blend. Specifically, for scalar function  $\lambda = \lambda(y, t)$  we define

$$(3.13) \quad \hat{s}_{\text{BLEND}}(\lambda) = \lambda \hat{s}_{\text{TWD}} + (1 - \lambda) \hat{s}_{\text{CSE}},$$

and note that  $\hat{s}_{\text{BLEND}}(\lambda)$  is unbiased for the true score  $s$ , since both  $\hat{s}_{\text{TWD}}$  and  $\hat{s}_{\text{CSE}}$  are unbiased estimators for  $s$ . The question is how to choose  $\lambda$  so that the blend  $\hat{s}_{\text{BLEND}}(\lambda)$  retains the complementary strengths of both estimators. Since the variance and correlation depend on  $(y, t)$ , we choose  $\lambda(y, t)$  to minimize the conditional variance of the blended error at  $(y, t)$ :

$$(3.14) \quad \lambda^*(y, t) \in \arg \min_{\lambda \in \mathbb{R}} J(\lambda; y, t), \quad J(\lambda; y, t) := \mathbb{E} \left[ \left\| \lambda \varepsilon_T + (1 - \lambda) \varepsilon_C \right\|^2 \right],$$

where  $\varepsilon_T := \hat{s}_{\text{TWD}} - \mathbb{E}[\hat{s}_{\text{TWD}}]$  and  $\varepsilon_C := \hat{s}_{\text{CSE}} - \mathbb{E}[\hat{s}_{\text{CSE}}]$ .

**PROPOSITION 3.5** (Variance-optimal blending weight). *Define*

$$\sigma_T^2 := \mathbb{E} \|\varepsilon_T\|^2, \quad \sigma_C^2 := \mathbb{E} \|\varepsilon_C\|^2, \quad \rho := \mathbb{E} \langle \varepsilon_T, \varepsilon_C \rangle.$$

*If  $\sigma_T^2 + \sigma_C^2 - 2\rho \neq 0$ , then the minimizer of (3.14) is unique and is given by*

$$(3.15) \quad \lambda^*(y, t) = \frac{\sigma_C^2 - \rho}{\sigma_T^2 + \sigma_C^2 - 2\rho}, \quad J(\lambda^*; y, t) = \frac{\sigma_T^2 \sigma_C^2 - \rho^2}{\sigma_T^2 + \sigma_C^2 - 2\rho}.$$

*Moreover, when  $\rho < 0$  (negative alignment of errors), the optimal weight satisfies  $0 < \lambda^*(y, t) < 1$  and the variance reduction is amplified as  $\rho$  becomes more negative.*

**Remark 3.6** (On variance vs. MSE). Under standard SNIS asymptotics, both bias and variance scale as  $\mathcal{O}(N_{\text{ref}}^{-1})$  [45–48], so for sufficiently large  $N_{\text{ref}}$  the MSE is often dominated by the variance. For that reason, we optimize  $\lambda$  by minimizing  $J(\lambda; y, t)$ .

In practice, we do not have access to  $\sigma_T$ ,  $\sigma_C$ , and  $\rho$ , at sampling time, only to their SNIS plug-in approximations. Specifically, with SNIS weights  $\tilde{w}_i$  we define

$$a_i := e^t s_0(x_0^i), \quad b_i := -\frac{1}{1 - e^{-2t}} (y - e^{-t} x_0^i),$$

$$\hat{s}_{\text{CSE}} = \sum_i \tilde{w}_i a_i, \quad \hat{s}_{\text{TWD}} = \sum_i \tilde{w}_i b_i.$$

We also define centered contributions  $\delta a_i = a_i - \hat{s}_{\text{CSE}}$  and  $\delta b_i = b_i - \hat{s}_{\text{TWD}}$ . The standard SNIS plug-in estimates are given

$$(3.16) \quad \hat{\sigma}_C^2 = \frac{\sum_i \tilde{w}_i^2 \|\delta a_i\|^2}{1 - \sum_i \tilde{w}_i^2}, \quad \hat{\sigma}_T^2 = \frac{\sum_i \tilde{w}_i^2 \|\delta b_i\|^2}{1 - \sum_i \tilde{w}_i^2}, \quad \hat{\rho} = \frac{\sum_i \tilde{w}_i^2 \langle \delta a_i, \delta b_i \rangle}{1 - \sum_i \tilde{w}_i^2} \frac{1}{\hat{\sigma}_T \hat{\sigma}_C}.$$

Plugging  $\hat{\sigma}_C^2$ ,  $\hat{\sigma}_T^2$  and  $\hat{\rho}$  into (B.4) yields the approximate blend weight  $\hat{\lambda}(y, t)$ .

We then define the corresponding SNIS plug-in blended score estimator using  $\hat{\lambda}$ :

$$(3.17) \quad \hat{s}_{\text{BLEND}}(y, t) := \hat{s}_{\text{BLEND}}(\hat{\lambda}(y, t)) = (1 - \hat{\lambda}(y, t)) \hat{s}_{\text{CSE}} + \hat{\lambda}(y, t) \hat{s}_{\text{TWD}}.$$

This blended score estimator forms the core of our non-parametric variance-minimizing sampling procedure in [Algorithm 3.1](#).

---

**Algorithm 3.1** Reverse Sampling optimal blend score

---

- 1: **Input:** Initial sampling particles  $\{y_j(T)\}_{j=1}^M \sim \mathcal{N}(0, I_d)$ , time grid  $T = t_K > \dots > t_0 = 0$ , reference data  $\{x_0^i, s_0(x_0^i)\}_{i=1}^{N_{\text{ref}}}$ , with  $x_0^i \sim p_0$ .
- 2: **for**  $k = K - 1, \dots, 0$  **do**
- 3:     Let current time be  $t_{k+1}$  and target time be  $t_k$ .
- 4:     **for**  $j = 1, \dots, M$  **do**
- 5:         Compute  $\hat{s}_{\text{BLEND}}(\hat{\lambda}(y_j(t_{k+1}), t_{k+1}))$  in [\(3.13\)](#) for particle  $y_j$ .
- 6:         Update particle  $y_j(t_k)$  using SDE integrator with  $\hat{s}_{\text{BLEND}}(\hat{\lambda}(y_j(t_{k+1})))$ .
- 7:     **end for**
- 8: **end for**
- 9: **Output:** Final samples  $\{y_j(0)\}_{j=1}^M$ .

---

**3.5. A learned proxy for the initial score.** When only i.i.d. samples  $X = \{x_0^i\}_{i=1}^{N_{\text{ref}}} \sim p_0$  are available, [Algorithm 3.1](#) requires an approximation of the unknown initial score  $s_0(x) = \nabla_x \log p_0(x)$ . We construct a *local Gaussian score proxy*  $\hat{s}_0(x_0^i)$  at each anchor  $x_0^i$  by fitting a kernel-weighted Gaussian to its  $k$  nearest neighbors, a standard local nonparametric construction [\[49–51\]](#). Let  $\mathcal{N}_k(i)$  be the indices of the  $k$  nearest neighbors of  $x_0^i$  in  $X$ , set  $h_i^2 := \max_{j \in \mathcal{N}_k(i)} \|x_0^i - x_0^j\|^2$ , define weights  $k_{ij} \propto \exp(-\|x_0^i - x_0^j\|^2/(2h_i^2))$ , and normalize  $\tilde{k}_{ij} := k_{ij} / \sum_{\ell \in \mathcal{N}_k(i)} k_{i\ell}$ . With the weighted mean  $\mu_i := \sum_{j \in \mathcal{N}_k(i)} \tilde{k}_{ij} x_0^j$  and a local covariance model  $\Sigma_i$  (below), we set

$$(3.18) \quad \hat{s}_0(x_0^i) := \Sigma_i^{-1}(\mu_i - x_0^i).$$

We use two covariance families (and label experiments accordingly):

1. **Diagonal proxy (Diag).**  $\Sigma_i^{\text{DIAG}} := \text{diag}(v_{i,1}, \dots, v_{i,d}) + \tau_i I$ , giving

$$(3.19) \quad \hat{s}_0^{\text{DIAG}}(x_0^i) := (\Sigma_i^{\text{DIAG}})^{-1}(\mu_i - x_0^i).$$

Here  $v_{i,\ell}$  are local per-coordinate variances estimated from the  $k$ NN cloud and  $\tau_i > 0$  is a ridge/noise-floor parameter.

2. **Low-rank plus diagonal tail proxy (LR+D).**  $\Sigma_i^{\text{LR+D}} := V_i \Lambda_i V_i^\top + \text{diag}(\tau_{i,1}, \dots, \tau_{i,d})$ , giving

$$(3.20) \quad \hat{s}_0^{\text{LR+D}}(x_0^i) := (\Sigma_i^{\text{LR+D}})^{-1}(\mu_i - x_0^i).$$

Here  $V_i \in \mathbb{R}^{d \times r}$  and  $\Lambda_i \in \mathbb{R}^{r \times r}$  capture the leading  $r$ -dimensional local principal subspace (e.g., via weighted PCA), and the diagonal tail ensures invertibility.

All further implementation details (weighting/bandwidth choices, optional query-time recomputation, and complexity considerations) are deferred to [Appendix C](#).

**3.6. Application to Bayesian Inverse Problems.** We adapt our framework to posterior sampling in inverse problems. Given a prior  $p_0(x)$ , likelihood  $L(y_{\text{obs}} | x)$  for an observation  $y_{\text{obs}}$ , the posterior is given by

$$\pi(x) \propto p_0(x) L(y_{\text{obs}} | x).$$

As is standard in inverse problems [52, 53], it is typically straightforward to sample the prior  $p_0$  but not the posterior. We therefore reuse the same prior reference set  $\{x_0^i\}_{i=1}^{N_{\text{ref}}}$  and *tilt* weights by the likelihood.

We assume that the observation  $y_{\text{obs}}$  depends on the unknown  $X_0$  but is independent of the forward OU corruption noise. This includes the common linear–Gaussian case  $y_{\text{obs}} = HX_0 + \varepsilon$  with  $\varepsilon \sim \mathcal{N}(0, \Sigma_y)$ , and more generally any  $L(y_{\text{obs}} \mid x_0)$  that does not involve the OU noise used to generate  $X_t$ . If this assumption were violated, the likelihood would depend on the diffusion path, preventing the factorization below and requiring joint path-space inference.

For a query point  $(x, t)$ , we update the OU transition weights by the likelihood to obtain posterior-tilted normalized weights [31, 32]

$$(3.21) \quad \alpha_i(y, t; y_{\text{obs}}) := \frac{w_i(y, t) L(y_{\text{obs}} \mid x_0^i)}{\sum_{j=1}^{N_{\text{ref}}} w_j(y, t) L(y_{\text{obs}} \mid x_0^j)}, \quad w_i(y, t) = K_t(y \mid x_0^i).$$

Equivalently,  $\{\alpha_i(y, t; y_{\text{obs}})\}$  are the SNIS weights for expectations under the tilted OU posterior  $p_{t|0}^{\text{post}}(x_0 \mid y) \propto p_0(x_0) L(y_{\text{obs}} \mid x_0) K_t(y \mid x_0)$ , approximated using the fixed prior reference set.

Using (3.21) together with the OU transition, we obtain a family of *posterior* score estimators. First, the posterior initial score decomposes as

$$s_0^{\text{post}}(x) := \nabla_x \log \pi(x) = s_0(x) + \nabla_x \log L(y_{\text{obs}} \mid x).$$

This leads to two natural estimators at time  $(y, t)$ . The Tweedie-type estimator is

$$\hat{s}_{\text{TWD}}^{\text{post}}(y, t) = -\frac{1}{1 - e^{-2t}} \sum_{i=1}^{N_{\text{ref}}} \alpha_i(y, t; y_{\text{obs}}) (y - e^{-t} x_0^i),$$

while the CSE-type estimator replaces the explicit OU drift term by a weighted average of the posterior initial scores:

$$\hat{s}_{\text{CSE}}^{\text{post}}(y, t) = e^t \sum_{i=1}^{N_{\text{ref}}} \alpha_i(y, t; y_{\text{obs}}) s_0^{\text{post}}(x_0^i).$$

As in the prior (untilted) case, the two estimators typically exhibit anti-aligned Monte Carlo fluctuations when computed from the same SNIS batch. We therefore form a convex combination with a batch-estimated weight chosen to minimize the plug-in variance using the same coefficients  $\alpha_i(y, t; y_{\text{obs}})$ :

$$\hat{s}_{\text{BLEND}}^{\text{post}}(y, t) = (1 - \lambda_{\text{snis}}^{\text{post}}) \hat{s}_{\text{CSE}}^{\text{post}}(y, t) + \lambda_{\text{snis}}^{\text{post}} \hat{s}_{\text{TWD}}^{\text{post}}(y, t).$$

Empirically, the anti-correlation mechanism persists under posterior tilting and is often strongest at intermediate diffusion times (see Appendix subsection E.1).

**4. Results.** We present numerical experiments that (i) validate the statistical claims underpinning our framework and (ii) demonstrate how variance reduction translates into improved downstream sampling fidelity. The experiments are organized to move from fully controlled settings, where ground truth scores and errors are accessible, to challenging inverse problems.

We begin with *results on a low-dimensional manifold* (subsection 4.1), using closed-form Gaussian mixture models where ground truth scores are available. In this

setting we compare Tweedie, CSE, and Blend across quantitative divergence metrics and qualitative PCA marginals, and we directly measure Monte Carlo errors as a function of the reference set size  $N_{\text{ref}}$  (Figure 4.2, Figure 4.1). We then conduct the regime sweep in subsection 4.2 to map out the “advantage regime”—the combinations of dimension and noise level where the blended score estimator  $\hat{s}_{\text{BLEND}}$  (3.17) yields the largest improvements in curvature and mass fidelity. Finally, we turn to inverse problems (subsection 4.3.1, subsection E.2), where we evaluate posterior sampling fidelity under (i) scientific forward operators with exact priors and (ii) image inverse problems with learned score proxies. Full details on hyperparameters, architectures, and experimental setups are provided in section F; full metric definitions and kernel/bandwidth choices are deferred to the appendix.

Unless stated otherwise, in *all* sampling tests we integrate the reverse-time dynamics with the *second order Heun predictor–corrector* (PC) solver (a standard choice in score-based SDE samplers; see, e.g [2]..). The same solver and time grid are used for Tweedie, CSE, and Blend to ensure comparability. In our experiments, samplers are evaluated along a log-spaced diffusion time grid  $t \in [t_{\min}, t_{\max}] = [5 \times 10^{-4}, 1.5]$ . The lower bound  $t_{\min}$  ensures that the OU noise level  $\sigma_t = \sqrt{1 - e^{-2t}}$  remains small enough to resolve fine structure while avoiding catastrophic importance-weight collapse at small  $t$ . The upper bound  $t_{\max}$  is large enough that  $p_t$  is close to the standard normal prior. The log spacing in  $t$  allocates more grid points to the small- $t$  regime where the score varies most rapidly and the actual sampling is carried out. For CSE (and hence Blend) we estimate conditional expectations via SNIS with an ESS threshold<sup>1</sup>.

**4.1. Moderate-dimensional manifold: 6D helix GMM.** We test the ability of the samplers to capture a complex, low-dimensional manifold embedded in a higher-dimensional space. The target is a 6D Gaussian Mixture Model (GMM) whose intrinsic structure is a 3D helix, shown in Figure 4.3. Unless stated otherwise, all quantitative loss curves in this section are computed on this **same 6D helix GMM**. In the qualitative panels (e.g., Figure 4.3), the point clouds represent samples drawn from the corresponding method (or from the ground-truth density) and projected onto the indicated principal directions; we never visualize score vectors directly. For visualization, we project samples onto two orthogonal planes  $(d_1, d_2)$ ,  $(d_3, d_4)$ , where  $d_1, \dots, d_4$  denote the first four principal directions obtained by PCA fit to the *target* distribution (fixed once for all methods). This axis selection highlights high-variance structure and does not *a priori* favor Blend over Tweedie (or vice versa). All concrete values (number of components, helix pitch/radius, covariance anisotropy, bandwidth grids, SNIS batch sizes, and the  $t$ -grid) are provided in section F.

**Quantitative comparisons.** To compare these estimators quantitatively, we use three complementary metrics that emphasize global mass placement, score-based discrepancy, and pointwise score error on the **same 6D helix GMM**: (i) MMD with an RBF kernel, which primarily reflects *global mass placement and coverage*; (ii) KSD with an inverse multiquadric kernel, a *score-based discrepancy* that is sensitive to both location and local geometry through the target score; and (iii) time-averaged score RMSE along the sampling  $t$ -grid, which measures *pointwise score error* along the diffusion path (ground-truth  $s$  is available for the GMM). We vary the number of

---

<sup>1</sup>We quantify importance-sampling quality via the effective sample size  $\text{ESS} = 1 / \sum_i \tilde{w}_i^2$ , where  $\tilde{w}_i$  are normalized SNIS weights. We drop time points with  $\text{ESS} < \tau_{\text{ESS}}$ , and in all experiments we set  $\tau_{\text{ESS}} := 0.05 N_{\text{ref}}$ .

reference samples  $N_{\text{ref}}$  to produce the curves in [Figure 4.1](#) and [Figure 4.2](#). Full definitions, estimator details, and kernel/bandwidth choices are deferred to the appendix; implementation details are provided in [section F](#).

In the following, by *Blend* (or *Blend Score*, solid blue curves), we mean the results obtained with the blended score estimator  $\hat{s}_{\text{BLEND}}$  (3.17) using the exact initial score  $s_0$ ; this serves as the oracle reference for the practical *Blend (proxy)* (dashed blue curves), which replaces  $s_0$  by the diagonal (Diag) learned local score proxy from [subsection 3.5](#). We also include the pure CSE estimator (green curves) in [Figure 4.1](#) and [Figure 4.2](#). In [Figure 4.1](#) (left), Blend (proxy, dashed blue) retains global mass placement in Tweedie, while in [Figure 4.1](#) (right) it achieves lower KSD than Tweedie, thanks to the local feature captured by CSE. In [Figure 4.2](#) the RMSE Blend (proxy, dashed blue) is at least an order of magnitude smaller than that of Tweedie. Due to its inability to resolve global structure, the pure CSE score estimator generally performs the worst, particularly on transport metrics like MMD. However, it performs better on local metrics (KSD and score RMSE) than on transport metrics, confirming that it provides a valid local gradient signal, and hence local fine structures that are exactly missed by Tweedie, even if it fails to coordinate global mass placement.

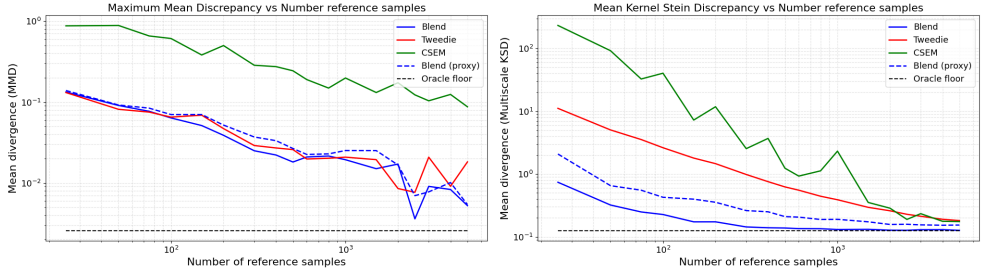


**FIG. 4.1. MMD and KSD vs. number of references (lower is better) on the 6D helix GMM.** **Left:** MMD with an RBF kernel, reflecting global mass placement and coverage. **Right:** KSD with an inverse multiquadric kernel, a score-based discrepancy sensitive to local geometry through the target score. Blend (proxy, dashed blue, using the diagonal learned score proxy from [subsection 3.5](#)) is comparable with Tweedie in terms of global mass placement (left), while achieving lower KSD than Tweedie (right). The oracle Blend (solid blue, using exact  $s_0$ ) further approaches the ground-truth floor. While CSE (green) shows high variance, the blended score estimators  $\hat{s}_{\text{BLEND}}$  (3.17) stabilize it.

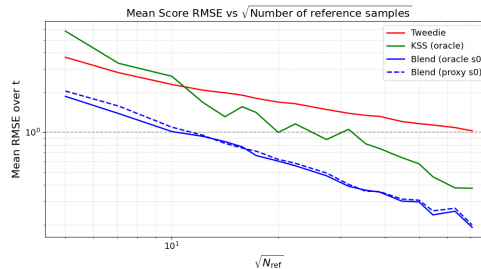


**FIG. 4.2. Time-averaged Score RMSE vs.  $\sqrt{N_{\text{ref}}}$  on the 6D helix GMM.** The RMSE Blend (proxy, dashed blue, diagonal learned score proxy from [subsection 3.5](#)) is similar to the oracle Blend (solid blue, exact  $s_0$ ), and it is at least an order smaller than that from Tweedie. Pure CSE (green) also achieves low RMSE at high sample counts, validating its local geometric accuracy, but fails to translate this into global transport (see [Figure 4.1](#)).

These three metrics paint a consistent picture that supports our blending strategy in [subsection 3.4.3](#): variance-minimal blending inherits the strengths of both estimators. Most of these gains are preserved even when the CSE term uses a score proxy fitted only to data, indicating that data-dependent curvature information extracted from raw samples is sufficient to deliver measurable improvements over Tweedie alone.

**Qualitative comparison.** We compare five columns: *True* (target samples), *Blend score (True)*—which uses the exact target score ( $s_0$ ) inside the variance-optimal blend, *Blend score (Proxy)*—which replaces  $s_0$  by the LR+D local Gaussian score proxy from [subsection 3.5](#) fit directly to the raw reference data, *Tweedie score* (standard nonparametric baseline), and *CSE score* in isolation. The results in [Figure 4.3](#) show that Blend (proxy) closely matches Blend (true), and both are nearly indistinguishable from the localized, complex ground truth across both PCA marginals. In contrast, Tweedie accurately resolves global scale position information but locally collapses generated samples onto a neighborhood around the reference samples, failing to capture the actual smooth local manifold structure. The CSE estimator, by directly leveraging  $s_0$ , captures fine-scale curvature and high-frequency geometric structure, but its higher variance at larger diffusion times can distort the induced distribution in “noise space,” which then manifests as misplaced probability mass after pushing back to  $t = 0$ . The variance-optimal Blend resolves these complementary failure modes by combining Tweedie’s stable global mass placement with CSE’s local geometric fidelity, yielding high-quality sampling that neither estimator achieves alone.

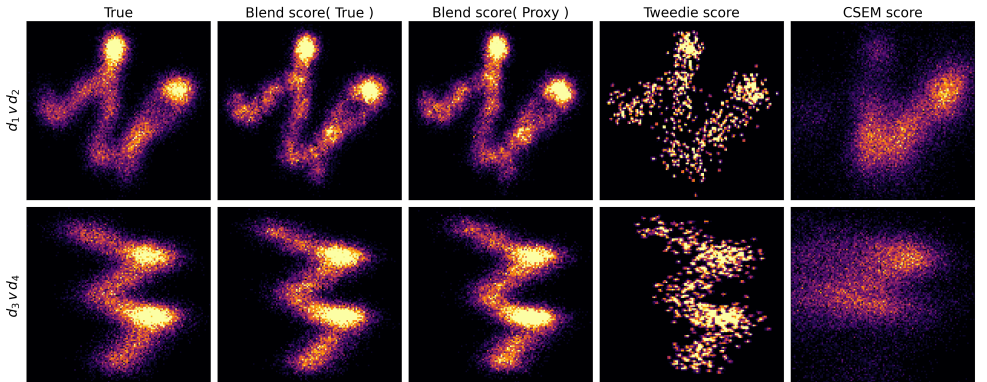


FIG. 4.3. *Qualitative comparison on the 6D helix GMM ( $N = 750$ )*. Each panel displays a 2D histogram of samples projected onto the principal directions  $(d_1, d_2)$  (top row) and  $(d_3, d_4)$  (bottom row), with PCA fitted to the target distribution and held fixed across methods. Columns show the True distribution, Blend score (True), Blend score (Proxy) using the LR+D proxy from [subsection 3.5](#), Tweedie score, and CSE score.

**4.2. Characterizing the Posterior Sampling Advantage Regime.** Before turning to the PDE and imaging inverse problems ([subsections 4.3.1](#) and [E.2](#)), we study the signal-to-noise ratio (SNR) regimes in which the variance-minimizing blend improves over the Tweedie baseline in a fully controlled setting with an *exact posterior* and *exact score*. In the regime sweep in [Fig. 4.4](#), we find that: (i) both methods struggle at high SNR (sharply concentrated likelihood) due to weight degeneracy; (ii) both methods become comparable when data are noisy (posterior close to the prior); and (iii) there is an intermediate-noise, moderate-dimension regime where the blend achieves appreciably lower sampling error than the tweedie based sampler.

Importantly, we also expose a *high-dimensional failure mode*. In this regime, both

approaches weaken, but the blended score estimator  $\hat{s}_{\text{BLEND}}$  (3.17) degrades further than the baseline. This is because the blend is “double leveraged” on quantities that become unstable in high dimensions—specifically, the collapse of SNIS weights and the difficulty of resolving optimal variance-minimization weights (3.16). This finding justifies truncating to a moderate number of KL/PCA modes in our subsequent experiments to remain within the advantageous regime.

**Synthetic inverse problem family (linear–Gaussian likelihood with a GMM prior).** For each dimension  $d \in \{3, 6, 12, 24\}$  we consider

$$(4.1) \quad x \sim p_0(x), \quad y_{\text{obs}} \mid x \sim \mathcal{N}(Ax, \sigma^2 I),$$

where  $p_0$  is a Gaussian mixture prior (GMM) in  $\mathbb{R}^d$ , and  $A : \mathbb{R}^d \rightarrow \mathbb{R}^d$  is a fixed linear “forward operator” with a non-trivial spectrum (chosen to mimic the anisotropy/ill-conditioning typical of inverse problems; details are fixed in the sweep script and held constant across the sweep). For each trial we draw a fresh latent truth  $x^* \sim p_0$  and observation noise  $\varepsilon \sim \mathcal{N}(0, I)$  and set  $y_{\text{obs}} = Ax^* + \sigma\varepsilon$ . The exact inverse problem setup details layed out in to [section F](#). Because the prior is a GMM and the likelihood is Gaussian, the posterior  $p(x \mid y_{\text{obs}})$  is again a (renormalized) GMM with the same number of components. This allows us to (i) draw *exact* posterior samples and (ii) evaluate the *exact posterior score*

$$(4.2) \quad \begin{aligned} s^*(x) &= \nabla_x \log p(x \mid y_{\text{obs}}) = \nabla_x \log p_0(x) + \nabla_x \log p(y_{\text{obs}} \mid x), \\ \nabla_x \log p(y_{\text{obs}} \mid x) &= \frac{1}{\sigma^2} A^\top (y_{\text{obs}} - Ax). \end{aligned}$$

**Dimension-coherent noise normalization (inverse SNR coordinate).** A recurring ambiguity in regime plots is that the *meaning* of “ $\sigma$ ” changes with dimension and with the operator  $A$  (since  $\|Ax\|$  is dimension- and spectrum-dependent). To make the horizontal axis comparable across  $d$ , we sweep a dimensionless, *dimension-coherent* inverse-SNR parameter  $\sigma_{\text{rel}} := \frac{\sigma}{\sqrt{\mathbb{E}_{x \sim p_0} \|Ax\|^2}}$ . The denominator is a signal scale induced by the prior and the forward map. In practice we estimate  $\sqrt{\mathbb{E}\|Ax\|^2}$  once per dimension by Monte Carlo under  $p_0$  (and keep it fixed throughout the sweep). We then sweep  $\sigma_{\text{rel}} \in [0.025, 1.0]$  on a log grid. Smaller  $\sigma_{\text{rel}}$  corresponds to higher SNR (sharper likelihood); larger  $\sigma_{\text{rel}}$  corresponds to a weaker data term (posterior closer to the prior).

We benchmark our proposed variance-minimizing blend score against a standard SNIS Tweedie baseline. To ensure a direct comparison, both estimators operate on the same reference set and utilize identical SNIS posterior weights. We strictly control the generation process by fixing the reference budget at  $N_{\text{ref}} = 4000$  and employing a shared Heun predictor–corrector sampler with matched time grids and sample counts ( $N_{\text{gen}}$ ). This rigorous alignment isolates the score estimator as the sole variable, ensuring that any performance differences are attributable strictly to the blend’s statistical properties rather than discrepancies in samplers or compute budgets.

We report the Gaussian-kernel MMD between generated and exact posterior samples in log scale, normalized by a per-setting *floor*:  $\log(\text{MMD}/\text{floor})$ . The floor is the MMD between two independent sets of exact posterior samples of the same size, and it captures the intrinsic finite-sample resolution of the metric in that setting; normalizing by it factors out dimension- and sample-size effects that would otherwise obscure regime transitions. Full metric definitions and kernel/bandwidth choices are deferred to appendix [section F](#).

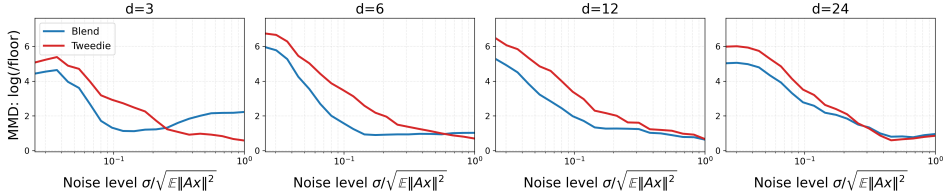


FIG. 4.4. *Regime sweep on the synthetic linear inverse family (4.1).* We plot  $\log(\text{MMD}/\text{floor})$  versus the dimension-coherent inverse-SNR parameter  $\sigma_{\text{rel}}$  in (4.2) (left is higher SNR), for  $d \in \{3, 6, 12, 24\}$ . Blue: Blend. Red: Tweedie baseline. The y-axis limits are the same for all panels.

Figure 4.4 cleanly separates three behaviors that mirror what we observe in the downstream inverse problems:

1. **High-SNR breakdown (small  $\sigma_{\text{rel}}$ ).** When the likelihood is sharply concentrated relative to the forward signal scale, both methods suffer (large  $\log(\text{MMD}/\text{floor})$ ). This is the controlled analogue of the “small-noise” instability observed in the real inverse problems, where importance weighting and finite reference budgets lead to weight degeneracy and high variance.
2. **Intermediate-noise advantage window (moderate  $\sigma_{\text{rel}}$ ).** For moderate dimensions ( $d = 3, 6$ , and  $12$ ), there is a visibly intermediate band of  $\sigma_{\text{rel}}$  where the Blend curve lies below Tweedie on MMD. This is the regime in which the posterior is informative enough that Tweedie-only bias/variance is exposed, but not so sharp that all reference-based estimators collapse.
3. **High-noise saturation / crossover (large  $\sigma_{\text{rel}}$ ).** As  $\sigma_{\text{rel}}$  increases and the posterior becomes less informative, the curves approach the MMD floor and (in the lowest-dimensional case) may cross, indicating that the benefit of blending is concentrated in the intermediate-noise window rather than in the prior-dominated limit.

The regime characterization in Figure 4.4 directly guides the parameter selection for the scientific and imaging inverse problems presented in subsequent sections. We specifically prioritize intermediate noise regimes, as this window—situated between the extremes of likelihood-dominated collapse and prior-dominated equivalence—is where the blended score estimator  $\hat{s}_{\text{BLEND}}$  (3.17) demonstrates the largest gains in our sweep. Concurrently, to mitigate the known sensitivity of reference-based estimation to increasing dimension at fixed computational budgets, we explicitly control the effective dimensionality. In our PDE and imaging experiments, we truncate the solution space to a moderate number of principal modes (e.g., 8–16), ensuring the solver operates within the stable capabilities identified in our sweep rather than in a regime dominated by sampling error.

**4.3. Inverse problems.** We conclude with inverse problems that probe posterior sampling fidelity in settings with (i) a *white-box* prior/likelihood, where the posterior density and score are available (up to normalizing constants), and (ii) a *black-box* prior, where the prior is accessible only through samples and must be represented by score proxies. These two regimes naturally support different diagnostics: in the white-box setting we can directly evaluate score-based discrepancies (e.g., KSD) and KL-type surrogates, while in black-box settings we rely on sample-based reference posteriors and distributional comparisons (e.g., MMD).

Across both problems we work in a reduced coordinate representation  $\alpha$  (KL coefficients for Navier–Stokes and PCA coefficients for MNIST), and map posterior sam-

ples back to the ambient space to evaluate reconstructed fields/images. We compare the Tweedie-only posterior sampler ( $\hat{s}_{\text{TWD}}$ ) against the variance-minimized blended posterior sampler ( $\hat{s}_{\text{BLEND}}$ ), formed by posterior tilting as in [subsection 3.6](#). Reference posteriors are obtained by MALA in the white-box setting (exact posterior target), and by importance sampling (IS) on a large held-out pool in the black-box setting. Full metric definitions are deferred to the appendix. Additional posterior-sampling diagnostics, including the inverse heat-equation experiment and extra MNIST visualizations, are deferred to [Appendix subsection E.2](#).

To make the two inverse problems as comparable as possible, we report a common core of metrics in both cases: (i) coordinate-space mean error  $\text{RMSE}_\alpha$  (root mean squared error), measuring the error of the posterior mean in coefficient space; (ii) ambient-space mean error  $\text{RMSE}_{\text{amb}}$ , measuring the error of the posterior mean after mapping back to the full field/image; and (iii) MMD to a reference posterior proxy (MALA for Navier–Stokes and IS for MNIST), which reflects *global distributional mismatch* to a high-quality baseline. In addition, we report a forward/data-fit error, measuring how well the posterior mean explains the noiseless observation through the forward operator. Precise definitions and normalization conventions are deferred to [section F](#).

**4.3.1. Navier–Stokes inverse problem (white-box posterior).** We evaluate the proposed posterior score estimators in a non-linear setting using the 2D Navier–Stokes equations on the torus  $\mathbb{T}^2 = [0, 2\pi]^2$ . Here we test the upper bound of the advantage regime by increasing the observation noise to  $\sigma_{\text{obs}} = 0.3$ , while maintaining a moderate latent dimension ( $d = 24$  eigenmodes). The system governs the evolution of the vorticity field  $w(x, t)$  according to

$$\partial_t w + u \cdot \nabla w = \nu \Delta w + f, \quad -\Delta \psi = w, \quad u = \nabla^\perp \psi,$$

where  $\nu$  is the viscosity,  $f$  is a forcing term, and  $u$  is the incompressible velocity field derived from the streamfunction  $\psi$ . The parameter of interest is the initial vorticity  $w_0(x)$ . We assume a sparse observation model where we measure the velocity field at 25 spatial locations (yielding 50 scalar observations) at a final time  $T$ . The observations  $y \in \mathbb{R}^{50}$  are given by  $y = \mathcal{O}(u(\cdot, T)) + \eta$ , with Gaussian noise  $\eta \sim \mathcal{N}(0, \sigma_{\text{obs}}^2 I)$  where  $\sigma_{\text{obs}} = 0.3$ .

**Posterior sampling formulation (prior, likelihood, score).** We work in a reduced Karhunen–Loève parameterization of the initial vorticity,

$$w_0(x; \alpha) = \sum_{i=1}^q \sqrt{\lambda_i} \phi_i(x) \alpha_i, \quad \alpha \in \mathbb{R}^q, \quad q = 24,$$

where  $(\lambda_i, \phi_i)$  are the leading eigenpairs of the prior covariance kernel. This yields a Gaussian prior on coefficients

$$p_0(\alpha) = \mathcal{N}(0, I), \quad s_0(\alpha) := \nabla_\alpha \log p_0(\alpha) = -\alpha,$$

and a Gaussian likelihood induced by the (differentiable) forward operator

$$F(\alpha) := \mathcal{O}(u(\cdot, T; w_0(\cdot; \alpha))) \in \mathbb{R}^{50}.$$

The target posterior distribution is defined as

$$p_{\text{post}}(\alpha \mid y) \propto p_0(\alpha) p(y \mid \alpha),$$

with posterior score at  $t = 0$  given by  $s_0^{\text{post}}(\alpha) = s_0(\alpha) + \nabla_\alpha \log p(y \mid \alpha)$ , where the likelihood gradient is obtained via the adjoint method (differentiable physics).

**Blended posterior score estimation.** Following subsection 3.6, we form posterior versions of the Tweedie and CSE estimators by tilting the SNIS logits by  $\log p(y \mid x_0^{(i)})$  and using  $s_0^{\text{post}}(x_0^{(i)})$  in the posterior correction. The proposed sampler ( $\hat{s}_{\text{BLEND}}$ ) uses the variance-optimal convex blend of these two estimators along the reverse trajectory, while  $\hat{s}_{\text{TWD}}$  uses the Tweedie term alone. We also compare against MALA targeting the exact posterior  $p_{\text{post}}(\alpha \mid y)$  as a reference baseline.

**Experimental setup and metrics.** We compare three sampling strategies: (i) the proposed blended posterior sampler ( $\hat{s}_{\text{BLEND}}$ ), (ii) the Tweedie-only posterior sampler ( $\hat{s}_{\text{TWD}}$ ), and (iii) MALA targeting  $p_{\text{post}}(\alpha \mid y)$  as a reference baseline. For  $\hat{s}_{\text{BLEND}}$  and  $\hat{s}_{\text{TWD}}$ , we use  $\mathcal{N} = 20,000$  reference coefficients  $\{x_0^{(i)}\}_{i=1}^{\mathcal{N}} \sim p_0$ , together with  $\{\log p(y \mid x_0^{(i)}), s_0^{\text{post}}(x_0^{(i)})\}$ , and generate samples with a Heun predictor–corrector integrator using 60 steps. For MALA, we run chains of 2,000 iterations with a burn-in of 500 steps.

We report the shared metrics (MMD→MALA,  $\text{RMSE}_\alpha$ ,  $\text{RMSE}_{\text{amb}}$ , and forward/data fit error), and additionally report KSD and  $\widetilde{\text{KL}}$  in this white-box setting. Here KSD is a score-based discrepancy that probes local geometric mismatch through the exact posterior score, while  $\widetilde{\text{KL}}$  is a KL-type diagnostic that reflects mismatch in posterior mass placement (precise estimators and normalizations are deferred to the appendix section F). Moment errors are omitted.

TABLE 4.1

**Navier–Stokes quantitative results.** Shared metrics (MMD→MALA, mean errors in coefficient/ambient space, and forward/data-fit error) are reported alongside KSD and  $\widetilde{\text{KL}}$ . Arrows indicate the preferred direction:  $\downarrow$  means lower values are better (all metrics reported here are minimized), with MALA serving as the reference for MMD→MALA.

Method	MMD→MALA $\downarrow$	$\text{RMSE}_\alpha \downarrow$	$\text{RMSE}_{\text{amb}} \downarrow$	Fwd Err $\downarrow$	KSD $\downarrow$	$\widetilde{\text{KL}} \downarrow$
Tweedie ( $\hat{s}_{\text{TWD}}$ )	0.1262	0.5819	0.1201	0.09847	15.80	94.68
Blend Posterior ( $\hat{s}_{\text{BLEND}}$ )	0.09022	0.5108	0.1114	0.1029	2.011	50.95
MALA (Reference)	0.0000	0.4776	0.1012	0.09550	1.774	42.25

We compare the Tweedie estimator ( $\hat{s}_{\text{TWD}}$ ), the Blend estimator ( $\hat{s}_{\text{BLEND}}$ ) and a standard MALA baseline. The results in Table 4.1 show that  $\hat{s}_{\text{BLEND}}$  corrects the approximation error of the pure Tweedie method: it matches the MALA-level KSD while maintaining runtime close to the low-cost Tweedie approximation.

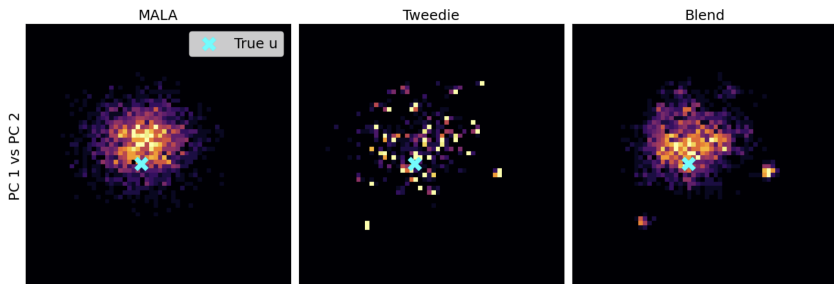


FIG. 4.5. **Posterior marginals.** 1D marginal distributions of the reconstructed vorticity values at selected spatial locations. The blended score estimator  $\hat{s}_{\text{BLEND}}$  (3.17) shifts the biased Tweedie distributions towards the ground truth posterior (MALA).

Visually, Figures 4.5 and 4.6 tell the same story:  $\hat{s}_{\text{BLEND}}$  yields posterior marginals and posterior-mean reconstructions and uncertainty maps that are substantially more consistent with those produced by the MALA reference.

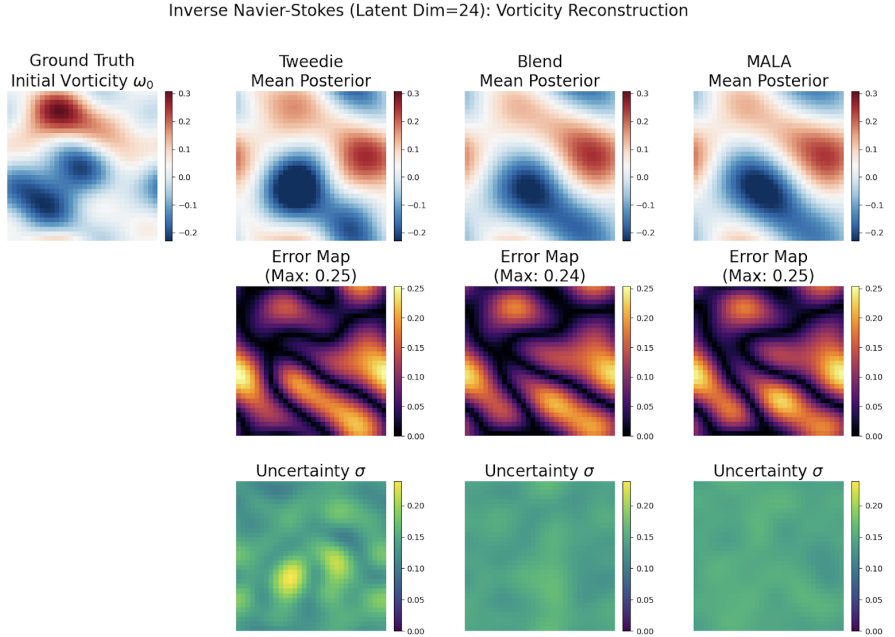


FIG. 4.6. *Navier–Stokes reconstruction.* Visual comparison of the posterior mean reconstruction of the initial vorticity  $w_0$ . The BLEND method recovers fine-scale vortex structures lost by the pure Tweedie estimator, closely approximating the MALA reference.

**4.3.2. MNIST deblurring inverse problem (black-box prior).** We conclude with a practical inverse problem: linear deblurring of MNIST digits. Unlike the Navier–Stokes inverse problem in subsection 4.3.1, where the prior score is known analytically, here the prior distribution  $p_0$  is unknown and accessible only through a finite set of samples. We define the problem in a reduced-order PCA latent space and estimate the score from these samples using the proposed blended proxy.

**Setup and latent space.** We utilize the MNIST training set (scaled to  $[0, 1]$ ) to compute a Principal Component Analysis (PCA) basis. We retain the top  $D = 15$  principal directions  $U_{15} \in \mathbb{R}^{784 \times 15}$  and mean  $\mu \in \mathbb{R}^{784}$ . Images are projected into this latent space via coefficients  $\alpha = U_{15}^\top(x - \mu) \in \mathbb{R}^{15}$ . The prior  $p_0(\alpha)$  is the implicit distribution of these coefficients. For score estimation, we use a reference set of  $N = 18,000$  such coefficients and fit the **LR+D proxy** (Section 3.5) directly in this 15-dimensional space.

**Observation model.** Observations  $y_{\text{obs}}$  are generated in the full image space by applying a  $9 \times 9$  Gaussian blur kernel  $H$  with standard deviation  $\sigma_{\text{blur}}=2.5$ , followed by additive white Gaussian noise  $\eta \sim \mathcal{N}(0, \sigma_{\text{obs}}^2 I)$ :  $y_{\text{obs}} = H(\mu + U_{15}\alpha) + \eta$ . This configuration targets the intermediate regime identified in Section 4.2 where variance reduction is most critical.

**Posterior sampling (implicit prior score + deblurring likelihood).** To obtain posterior samples for the MNIST deblurring problem, we follow the posterior

weight-tilting construction in [subsection 3.6](#), but with an *implicit* prior in the PCA coefficient space. Concretely, the prior  $p_0(\alpha)$  is represented by the reference set of MNIST PCA coefficients, and its score is provided either by the Tweedie estimator  $\hat{s}_{\text{TWD}}$  or by the SNIS plug-in blended estimator  $\hat{s}_{\text{BLEND}}$  defined in [\(3.17\)](#), where the CSE term uses the LR+D proxy fit to the raw MNIST data ([subsection 3.5](#)).

The observation model induces a linear–Gaussian likelihood

$$\mathcal{L}(\alpha) := p(y_{\text{obs}} \mid \alpha) = \mathcal{N}(y_{\text{obs}}; H(\mu + U_{15}\alpha), \sigma_{\text{obs}}^2 I),$$

with log-likelihood gradient (in  $\alpha$ -space)

$$\nabla_{\alpha} \log \mathcal{L}(\alpha) = \frac{1}{\sigma_{\text{obs}}^2} (H U_{15})^{\top} (y_{\text{obs}} - H(\mu + U_{15}\alpha)).$$

At sampling time, we form the posterior score estimator exactly as in [subsection 3.6](#): we tilt the SNIS weights by  $\mathcal{L}(\alpha_0^i)$  and use the resulting posterior version of the score estimator along the reverse trajectory. Final samples are mapped back to image space by  $x = \mu + U_{15}\alpha$ .

**Reference posterior and MCMC baseline.** Since the true posterior is intractable, we construct a “gold standard” reference distribution using importance sampling (IS) on a large held-out pool of prior samples. We also compare against a gradient-based MALA baseline targeting an approximate posterior built from a differentiable GMM surrogate prior in latent space (details as in appendix [section F](#)).

**Quantitative results.** We report the shared metrics (MMD→IS,  $\text{RMSE}_{\alpha}$ ,  $\text{RMSE}_{\text{amb}}$ , and forward/data-fit error) and, specific to the image setting, PSNR and Coverage. Here PSNR reflects image-space reconstruction quality (a monotone transform of pixel MSE), while Coverage measures whether generated samples fall within high-probability regions of the IS reference posterior. Precise definitions and normalization conventions are deferred to appendix [section F](#).

Method	PSNR (dB) $\uparrow$	Coverage (%) $\uparrow$	$\text{RMSE}_{\alpha} \downarrow$	$\text{RMSE}_{\text{amb}} \downarrow$	Fwd Err $\downarrow$	MMD→IS $\downarrow$
Blend (Proxy)	28.02	100.0	0.1550	0.0397	0.1152	0.1086
Tweedie only	26.98	92.6	0.1843	0.0448	0.1662	0.1876
MALA-GMM	25.99	100.0	0.1898	0.0502	0.1307	0.1324

TABLE 4.2

**MNIST deblurring metrics.**  $\uparrow$  means higher value is better (PSNR, Coverage), and  $\downarrow$  means lower is better ( $\text{RMSE}_{\alpha}$ ,  $\text{RMSE}_{\text{amb}}$ , Fwd Err, and MMD→IS). Blend (Proxy) improves posterior fidelity (Coverage, MMD) and image quality (PSNR); shared mean-error and forward-error metrics are reported for direct comparison to the Navier–Stokes inverse problem.

This difference is visually apparent in [Figure 4.7](#). The blended posterior aligns closely with the IS support, while Tweedie collapses onto a sparse set of reference training samples.

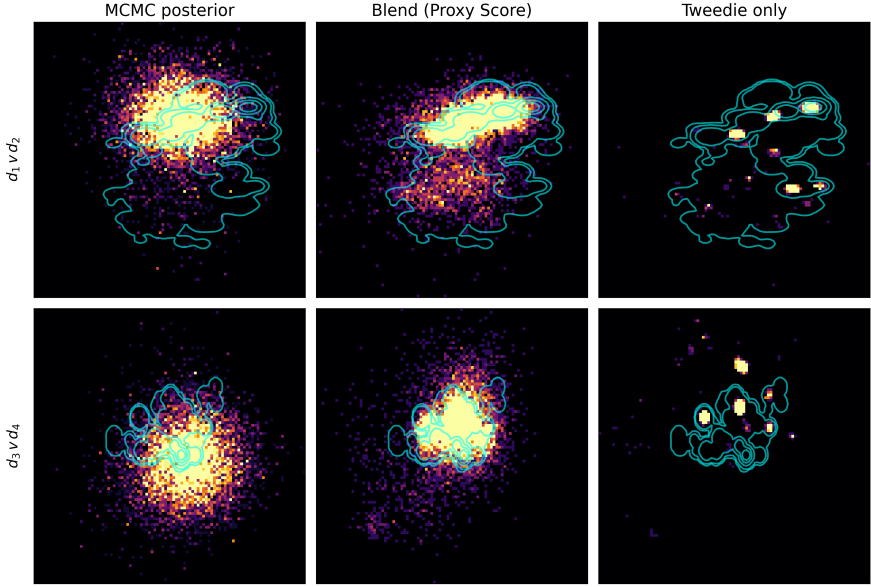


FIG. 4.7. *MNIST: likelihood pushes prior mass (PCA plane ( $d_1, d_2$ )).* Cyan IS contours denote HPD levels of the IS posterior. The blended posterior sample distribution aligns with these contours more closely than Tweedie, which collapses onto a sparse set of reference points.

More MNIST posterior-sampling visualizations (including a multi panel sample comparison) are provided in Appendix subsection E.2.

**5. Discussion.** Our primary contributions in this work are advancements to the *statistical estimation of score fields* for diffusion/flow models. Rather than proposing a new reverse solver or sampler architecture, we improve the *local score signal* itself. We demonstrate that the blended score estimator  $\hat{s}_{\text{BLEND}}$  (3.17) yields a lower-variance signal by exploiting the *negative correlation* between two complementary, semigroup-native estimators: Tweedie and CSE. Functionally, this blend manifests as a natural **multiscale decomposition of transport**. The Tweedie estimator acts as a *global transport operator*, moving mass reliably at large diffusion times ( $t \gg 0$ ) based on coarse cluster information. Conversely, CSE acts as a *local transport operator*, resolving fine-scale curvature and tangent gradients at small times ( $t \rightarrow 0$ ). The variance-minimizing blend weight  $\lambda^*(y, t)$  acts as an automatic gate, smoothly interchanging between these two regimes to minimize risk. The result is improved computational efficiency and improved sampling fidelity, driven by lower-variance estimation of the underlying geometry.

A practical interpretation of CSE is that it performs *local data augmentation* by propagating neighborhood curvature. While standard estimators view reference samples as Dirac masses, CSE utilizes local Gaussian score proxies (DIAG or LR+D; see subsection 3.5) to model the *shape* of the distribution around each point. This effectively bridges the gap between discrete training samples, artificially increasing the Effective Sample Size (ESS) in the local neighborhood of the query. This explains the intermediate regime identified in our regime study (subsection 4.2): the estimator shows the largest gains in regimes where the diffusion noise scale is sufficient to overlap these local curvature proxies, allowing the blend to reconstruct the manifold geometry even when the finite reference set is sparse. By explicitly modeling these local gradients, CSE reduces the geometric bias inherent in standard nonparametric

approximations.

Our investigation into inverse problems reveals that the Tweedie estimator’s tendency to collapse is exacerbated in posterior sampling. As shown in the regime sweep in subsection 4.2 (Fig. 4.4), this performance gap widens as the observation noise decreases (increasing likelihood sharpness) and as the latent dimension increases. This pathology arises from a “Double Jeopardy” variance trap that the blended score estimator  $\hat{s}_{\text{BLEND}}$  (3.17) escapes.

At large diffusion times, the dominant failure mode is weight collapse: the self-normalized importance sampling (SNIS) weights for the posterior differ from the prior weights by the likelihood term,

$$\tilde{w}_i^{\text{post}} \propto K_t(y \mid x_0^{(i)}) \cdot \mathcal{L}(y_{\text{obs}} \mid x_0^{(i)}).$$

In high-dimensional inverse problems,  $\mathcal{L}(y_{\text{obs}} \mid x)$  concentrates mass on a thin manifold. When using a fixed reference set from a diffuse prior, the ESS degrades rapidly. In the limit ( $\text{ESS} \rightarrow 1$ ), the estimator becomes dominated by the single reference particle  $x_0^{(k)}$  maximizing the likelihood-kernel product. Consequently, the score degenerates to  $\hat{s}_{\text{TWD}} \approx \sigma_t^{-2}(e^{-t}x_0^{(k)} - y)$ , acting as a linear restoring force toward a single training point rather than interpolating the posterior manifold (the “fragmented” memorization seen in Figure 4.7).

A second failure mode appears as  $t \rightarrow 0$ . Even though the likelihood gradient becomes sharp, Tweedie’s prior term scales like  $\sigma_t^{-2} \approx t^{-1}$ , so estimator noise dominates precisely in the small-time regime where the likelihood would otherwise help. While the likelihood signal  $\nabla \log \mathcal{L}$  becomes sharp at small  $t$ , the Tweedie estimator is statistically incapable of resolving it because the noise in the prior estimation dominates the signal. Thus, Tweedie fails at large  $t$  (due to weight collapse) *and* at small  $t$  (due to variance explosion).

CSE addresses this failure mode by carrying the likelihood gradient inside the transported estimate:

$$\hat{s}_{\text{CSE}}^{\text{post}}(y, t) \approx e^t(\hat{s}_0 + \nabla_{x_0} \log \mathcal{L}(y_{\text{obs}} \mid \hat{x}_0)).$$

Because the likelihood term is deterministic and the prefactor remains well behaved as  $t \rightarrow 0$ , this contribution stays low-variance in the small-time regime. the blended score estimator  $\hat{s}_{\text{BLEND}}$  (3.17) then uses CSE precisely where Tweedie becomes unstable, so the likelihood correction is injected at the times when it can be resolved statistically.

Beyond nonparametric sampling, a primary utility of this framework is generating an *augmented statistical signal* for training high-quality diffusion models. In both SciML settings (where the exact score is calculable but expensive) and pure ML settings (where the score is learned), the blended score estimator  $\hat{s}_{\text{BLEND}}$  (3.17) serves as a **low-variance teacher**. As detailed in the “Critic Gate” analysis (section D), distilling the blended target  $(y, t) \mapsto \hat{s}_{\text{BLEND}}(y, t)$  yields a stronger supervision signal than standard denoising objectives, filtering out high-variance outliers before they pollute the student network.

We with a discussion of the main practical limitations to our approach. In the most challenging inverse regimes—sharply concentrated likelihoods or high effective dimension—finite-reference reweighting can degenerate and the estimator becomes unstable. A second limitation is geometric: if the forward noise scale fails to overlap the local curvature proxies, local linear/quadratic corrections cannot reliably bridge gaps between sparse references. These issues motivate the scaling directions summarized in the conclusion.

**6. Conclusion and Future Work.** We reframed score learning as a *statistical estimation* problem at a queried  $(y, t)$  and introduced a semigroup-native estimator that combines two complementary signals. The key ingredient is the Conditional Score Expectation (CSE) identity, which transports score information across time through the forward semigroup. Using the Ornstein–Uhlenbeck (OU) flow as a canonical worked example, we derived an exact finite-time identity, constructed a nonparametric CSE estimator, and paired it with the classical Tweedie estimator. We proved (linear–Gaussian) and motivated (single-basin) negative alignment of their Monte Carlo errors, yielding a *variance-minimizing convex blend* with a closed-form weight  $\lambda^*(y, t)$ . An SNIS plug-in provides the quantities needed for  $\lambda^*$ , while local Gaussian score proxies (DIAG/LR+D; [subsection 3.5](#)) supply stable curvature information when ground truth  $s_0$  is unavailable. The same estimator extends to posterior inference by a one-line likelihood tilt of the SNIS weights. Although OU affords closed forms, the CSE viewpoint itself extends to *affine diffusions* via gradient–semigroup commutation; our claims and constructions are formulated with this generality in mind.

Our future roadmap keeps the estimator-centric viewpoint but moves toward neural implementations along three parallel tracks: distillation, scaling, and statistical robustness. First, we want a **neural distillation** of the blended score estimator itself. Concretely, we treat the CSE and Tweedie estimators as two unbiased (but differently noisy) training signals for the same target score, and we train a network to (i) predict the score and (ii) predict the blending weight by minimizing an MSE criterion that reflects the per-input variance tradeoff. In other words, rather than fixing a hand-designed blend schedule or supervising with a pre-averaged estimator, we learn the blend as part of the score-learning objective so that the network can adapt the mixture across diffusion time and across input locations. Appendix D contains a prototype of this joint learning procedure, which we refer to as the *Critic–Gate* method.

To scale these benefits to high-dimensional image and video benchmarks, we will move beyond simple Gaussian proxies by developing **curvature-aware embeddings**. These latent spaces—such as VAEs that expose local covariance—will allow the CSE transport machinery to operate at low computational cost within a compressed semantic geometry. Finally, to address the concentration barriers inherent in standard importance sampling, we will incorporate **stability-oriented sampling strategies** such as tempering, mixture proposals, and sequential Monte Carlo. These remedies aim to stabilize the plug-in variance estimates and the mixing weight  $\lambda^*(y, t)$  for concentrated posteriors. Across these directions, the objective remains the same: to deliver a *lower-variance local score estimate*—amortized by the critic and modulated by the gate—that downstream samplers and neural students can exploit for higher fidelity sampling given a fixed compute budget.

## Appendix A. Derivation of the CSE Identity for Linear/Affine SDEs.

We provide a statement and proof of the CSE identity (3.9) for general affine SDEs. To begin, we consider the time-inhomogeneous affine SDE on  $\mathbb{R}^d$  defined by

$$dX_t = A(t)X_t dt + b(t)dt + G(t)dW_t, \quad X_0 \sim p_0,$$

where  $A(t) \in \mathbb{R}^{d \times d}$ ,  $b(t) \in \mathbb{R}^d$ , and  $G(t) \in \mathbb{R}^{d \times r}$  are measurable and locally bounded functions, and  $W_t$  denotes an  $r$ -dimensional standard Brownian motion.

Let  $\Phi(t, s) \in \mathbb{R}^{d \times d}$  be the *fundamental matrix* associated with the linear ODE  $\dot{Z}(t) = A(t)Z(t)$ . It is the unique matrix function satisfying

$$\partial_t \Phi(t, s) = A(t)\Phi(t, s), \quad \Phi(s, s) = I_d.$$

In the time-homogeneous case where  $A(t) \equiv A$ , this matrix simplifies to  $\Phi(t, s) = e^{A(t-s)}$ .

It is well-known that the solution  $X_t$  constitutes a Gaussian process. The transition kernel  $K_t(y | x)$  takes the form

$\mathcal{N}(y; \Phi(t, 0)x + m(t), \Gamma(t))$ , where the mean offset  $m(t)$  and covariance  $\Gamma(t)$  are defined as

$$m(t) := \int_0^t \Phi(t, \tau)b(\tau)d\tau, \quad \Gamma(t) := \int_0^t \Phi(t, \tau)G(\tau)G(\tau)^\top \Phi(t, \tau)^\top d\tau.$$

We denote the score of the time- $t$  marginal density  $p_t(y)$  by  $s(y, t) := \nabla_y \log p_t(y)$  and the initial score by  $s_0(x) := \nabla_x \log p_0(x)$ . We assume that for each  $t > 0$ , the transition is nondegenerate (i.e.,  $\Gamma(t)$  is positive definite) and that the boundary terms vanish during integration by parts. Given these prerequisite definitions we can state and prove the CSE identity for general affine SDEs.

**THEOREM A.1** (CSE for Linear/Affine SDEs). *Consider any affine SDE satisfying the conditions outlined above. Then, for every  $t > 0$  and  $y \in \mathbb{R}^d$ , the score function satisfies*

$$(A.1) \quad s(y, t) = \Phi(t, 0)^{-\top} \mathbb{E}_{x_0 \sim p_{t|0}(\cdot | y)} [s_0(x_0)],$$

where  $p_{t|0}(x_0 | y) = p(x_0 | X_t = y)$  denotes the posterior distribution of the initial data given the noisy observation  $y$ .

*Proof.* The Gaussian transition kernel is given by

$$K_t(y | x) \propto \exp \left( -\frac{1}{2} \|y - (\Phi(t, 0)x + m(t))\|_{\Gamma(t)^{-1}}^2 \right).$$

Taking gradients with respect to  $y$  and  $x$  yields the following cross-derivative identity:

$$(A.2) \quad \nabla_y K_t(y | x) = -\Phi(t, 0)^{-\top} \nabla_x K_t(y | x).$$

By definition, the score is  $s(y, t) = \frac{\nabla_y p_t(y)}{p_t(y)}$ . Differentiating the marginal density  $p_t(y) = \int K_t(y | x)p_0(x)dx$  under the integral sign and applying the identity (A.2), we obtain

$$\nabla_y p_t(y) = \int \nabla_y K_t(y | x)p_0(x)dx = -\Phi(t, 0)^{-\top} \int \nabla_x K_t(y | x)p_0(x)dx.$$

Integrating the right-hand side by parts with respect to  $x$  gives

$$\int \nabla_x K_t(y | x) p_0(x) dx = - \int K_t(y | x) \nabla_x p_0(x) dx = - \int K_t(y | x) p_0(x) s_0(x) dx.$$

Substituting this result back into the expression for  $\nabla_y p_t(y)$ , we have

$$\nabla_y p_t(y) = \Phi(t, 0)^{-\top} \int K_t(y | x) p_0(x) s_0(x) dx = \Phi(t, 0)^{-\top} p_t(y) \mathbb{E}_{x_0 \sim p_{t|0}(\cdot | y)} [s_0(x_0)].$$

The proof is concluded by dividing both sides by  $p_t(y)$ .  $\square$

The standard OU process ((3.1)) corresponds to  $A(t) \equiv -I_d$ . In this case, the fundamental matrix is  $\Phi(t, 0) = e^{-t} I_d$ . Substituting this into the general identity ((A.1)) gives:

$$s(y, t) = (e^{-t} I_d)^{-\top} \mathbb{E}_{x_0 \sim p_{t|0}(\cdot | y)} [s_0(x_0)] = e^t \mathbb{E}_{x_0 \sim p_{t|0}(\cdot | y)} [s_0(x_0)],$$

which is exactly the identity presented in the main text in (3.9).

This generalized CSE identity applies to all common linear SDEs used in generative modeling. We consider the main canonical examples below

**I. Variance-Preserving (VP) SDE.** For  $dX_t = -\frac{1}{2}\beta(t)X_t dt + \sqrt{\beta(t)}dW_t$ , we have  $\Phi(t, 0) = \alpha(t)I$  where  $\alpha(t) = \exp(-\frac{1}{2} \int_0^t \beta(u) du)$ . The CSE identity is:

$$s(y, t) = \alpha(t)^{-1} \mathbb{E}_{x_0 \sim p_{t|0}(\cdot | y)} [s_0(x_0)].$$

**II. Variance-Exploding (VE) SDE.** For  $dX_t = g(t)dW_t$ , we have  $\Phi(t, 0) = I$ . The CSE identity is:

$$s(y, t) = \mathbb{E}_{x_0 \sim p_{t|0}(\cdot | y)} [s_0(x_0)].$$

**III. Anisotropic OU / Whitening SDE.** For  $dX_t = AX_t dt + GdW_t$  with constant matrices  $A$  and  $G$ , we have  $\Phi(t, 0) = e^{At}$ . The CSE identity is:

$$s(y, t) = e^{-A^\top t} \mathbb{E}_{x_0 \sim p_{t|0}(\cdot | y)} [s_0(x_0)].$$

**Note: Gradient–Semigroup Commutation (general affine case).** The relationship between the Tweedie perspective in subsection 3.2 and the CSE identity in (A.1) is governed by the **Gradient–Semigroup Commutation (GSC)** principle [33]. Let  $P_t$  denote the forward evolution (pushforward) operator acting on the initial density  $p_0$  via the affine transition kernel  $K_t$ , i.e.

$$(P_t p_0)(y) = p_t(y) = \int K_t(y | x) p_0(x) dx, \quad K_t(y | x) = \mathcal{N}(y; \Phi(t, 0)x + m(t), \Gamma(t)).$$

For affine diffusions, the Gaussian form implies the cross-derivative identity

$$\nabla_y K_t(y | x) = -\Phi(t, 0)^{-\top} \nabla_x K_t(y | x),$$

so differentiation under the integral sign and integration by parts yield the commutation rule

(A.3)

$$\nabla_y (P_t p_0)(y) = \Phi(t, 0)^{-\top} (P_t \nabla p_0)(y), \quad (P_t \nabla p_0)(y) := \int K_t(y | x) \nabla_x p_0(x) dx.$$

Dividing (A.3) by  $p_t(y) = (P_t p_0)(y)$  gives the corresponding identity for the score :

$$\nabla_y \log(P_t p_0)(y) = \Phi(t, 0)^{-\top} \mathbb{E}_{x_0 \sim p_{t|0}(\cdot | y)} [\nabla_{x_0} \log p_0(x_0)]$$

In words, smoothing the density and then taking a gradient in  $y$  is equivalent to taking the initial gradient field in  $x$  and then smoothing it against the posterior, with the linear prefactor  $\Phi(t, 0)^{-\top}$  determined by the drift. For the standard OU choice  $A(t) \equiv -I_d$ , we have  $\Phi(t, 0) = e^{-t}I_d$  and the prefactor reduces to  $e^t$ , recovering the OU-specific statement used in the main text.

## Appendix B. Proofs.

**B.1. Auxiliary results for the proof of Theorem 3.4.** The following result says that the condition distribution  $p_{t|0} := p_{t|0}(x | y)$  is strongly log-concave. This is obvious for all  $t$  if  $m(y) \geq 0$ , and thus we focus on the case when  $m(y) < 0$ .

LEMMA B.1 (Strongly log-concave of  $p_{t|0}(x | y)$  for small time when  $m(y) < 0$ ). *If  $t < \frac{1}{2} \log \left(1 - \frac{1}{m(y)}\right)$ , then  $p_{t|0}(x_0 | y)$  is strongly log-concave, meaning that:*

$$-\nabla_{x_0}^2 \log p_{t|0}(x_0 | y) \succeq \kappa(y) I \succ 0, \text{ where } \kappa(y) := m(y) + \frac{e^{-2t}}{1 - e^{-2t}},$$

and

$$\Sigma := \text{Cov}_{p_{t|0}}(X) \preceq \frac{1}{\kappa(y)} I.$$

*Proof.* From (3.5) we have

$$\begin{aligned} -\nabla_{x_0}^2 \log p_{t|0}(x_0 | y) &= -\nabla_{x_0}^2 [\log p_0(x_0)] + \frac{e^{-2t}}{1 - e^{-2t}} I \\ &\succeq \left(m(y) + \frac{e^{-2t}}{1 - e^{-2t}}\right) I \succeq \kappa(y) I \succ 0, \end{aligned}$$

for all  $t < \frac{1}{2} \log(1 - 1/m(y))$ . The second assertion is obvious by the Brascamp-Lieb inequality [54, 55].  $\square$

Now, define the truth condition mean as  $\mu := \mathbb{E}[X_0 | X_t = y]$ . Using a first-order Taylor expansion of the score  $s_0$  around  $\mu$  we have

$$s_0(x) = s_0(\mu) + \nabla s_0(\mu)(x - \mu) + f(x),$$

where

$$(B.1) \quad \|f(x)\| \leq c \|x - \mu\|^2, \text{ since } \|\nabla_x^3 [\log p_0(x)]\|_{op} \leq c.$$

As a result, the exact CSE score (3.10) is now given as

$$s_C(y, t) = e^t \mathbb{E}_{p_{t|0}}[s_0(X_0)] = e^t [s_0(\mu) + \mathbb{E}_{p_{t|0}}[f(X_0)]],$$

where, by Lemma B.1,

$$|\mathbb{E}_{p_{t|0}}[f(X_0)]| \leq \frac{c}{2} \mathbb{E}_{p_{t|0}}[\|X_0 - \mu\|^2] = \frac{c}{2} \text{Tr}(\Sigma) \leq \frac{cd}{2\kappa(y)},$$

which is small for small time  $t$  as  $\kappa \approx (2t)^{-1}$ . The SNIS estimator of  $s_C$  is

$$\hat{s}_C = e^t \left[ s_0(\mu) + \nabla s_0^T(\mu)(\hat{\mu} - \mu) + \hat{f} \right], \text{ where } \hat{\mu} = \sum_i \tilde{w}_i X_0^i, \text{ and } \hat{f} := \sum_i \tilde{w}_i f(X_0^i).$$

Consequently, the deviation of the SNIS CSE score is

$$\varepsilon_C = \hat{s}_C - s_C = e^t [\nabla s_0^T(\mu) \varepsilon_\mu + \varepsilon_f], \text{ where } \varepsilon_\mu = \hat{\mu} - \mu, \text{ and } \varepsilon_f = \hat{f} - \mathbb{E}_{p_{t|0}}[f(X_0)].$$

Similarly, the deviation of SNIS estimation of Tweedie is given by

$$\varepsilon_T = \hat{s}_T - s_T = \frac{e^{-t}}{1 - e^{-2t}} \varepsilon_\mu.$$

The correlation between CSE and Tweedie is thus

$$(B.2) \quad \mathbb{E}_{p_0} [\varepsilon_C^T \varepsilon_T] = - \underbrace{\frac{1}{1 - e^{-2t}} \mathbb{E}_{p_0} [\varepsilon_\mu^T \Sigma_{\text{eff}}^{-1} \varepsilon_\mu]}_D + \underbrace{\frac{1}{1 - e^{-2t}} \mathbb{E}_{p_0} [\varepsilon_f^T \varepsilon_\mu]}_E.$$

LEMMA B.2 (Bounding the dominant term  $D$ ). *There holds:*

$$D = \frac{1}{1 - e^{-2t}} \text{Tr} (\Sigma_{\text{eff}}^{-1} \text{Cov}_{p_0}(\hat{\mu})) \gtrsim \frac{1}{1 - e^{-2t}} \frac{w_{\min}}{N_{\text{ref}}} \lambda_{\min} (\Sigma_{\text{eff}}^{-1}) \|\Sigma\|_{\text{op}}.$$

*Proof.* Using the standard delta method and the central limit for SNIS [45–48] gives

$$(B.3a) \quad \text{Cov}_{p_0}(\hat{\mu}) = \frac{1}{N_{\text{ref}}} \Omega_\mu + o\left(\frac{1}{N_{\text{ref}}}\right) \quad \text{as } N_{\text{ref}} \rightarrow \infty,$$

where  $\Omega_\mu = \mathbb{E}_{p_{t|0}} [w(X_0) (X_0 - \mu)(X_0 - \mu)^\top]$ . Since the important weights are bounded, we obtain

$$\|\Omega_\mu\|_{\text{op}} \geq w_{\min} \|\Sigma\|_{\text{op}}.$$

Using (B.3) we have

$$\begin{aligned} \mathbb{E}_{p_0} [\varepsilon_\mu^T \Sigma_{\text{eff}}^{-1} \varepsilon_\mu] &= \text{Tr} (\Sigma_{\text{eff}}^{-1} \text{Cov}_{p_0}(\hat{\mu})) \geq \lambda_{\min} (\Sigma_{\text{eff}}^{-1}) \text{Tr} (\text{Cov}_{p_0}(\hat{\mu})) \\ &\gtrsim \lambda_{\min} (\Sigma_{\text{eff}}^{-1}) \frac{\text{Tr} (\Omega_\mu)}{N_{\text{ref}}} \gtrsim \frac{\lambda_{\min} (\Sigma_{\text{eff}}^{-1})}{N_{\text{ref}}} \|\Omega\|_{\text{op}} \gtrsim \frac{w_{\min}}{N_{\text{ref}}} \lambda_{\min} (\Sigma_{\text{eff}}^{-1}) \|\Sigma\|_{\text{op}}. \quad \square \end{aligned}$$

LEMMA B.3 (Bounding the cross term  $E$ ). *There holds:*

$$E \leq \frac{1}{1 - e^{-2t}} \frac{w_{\max}}{N_{\text{ref}}} \frac{cd}{\kappa} \sqrt{\text{Tr} (\Sigma)}.$$

*Proof.* Similar to (B.3a), we have

$$\text{Cov}_{p_0}(\hat{f}) = \frac{1}{N_{\text{ref}}} \Omega_f + o\left(\frac{1}{N_{\text{ref}}}\right) \quad \text{as } N_{\text{ref}} \rightarrow \infty,$$

where  $\Omega_f = \mathbb{E}_{p_{t|0}} [w(X_0) (f(X_0) - \mathbb{E}_{p_{t|0}}[f(X_0)]) (f(X_0) - \mathbb{E}_{p_{t|0}}[f(X_0)])^\top]$ . By Cauchy-Schwarz inequality we have

$$\begin{aligned} \mathbb{E}_{p_0} [\varepsilon_f^T \varepsilon_\mu] &\leq \sqrt{\text{Tr} (\text{Cov}_{p_0}(\hat{f}))} \sqrt{\text{Tr} (\text{Cov}_{p_0}(\hat{\mu}))} \\ &\lesssim \frac{w_{\max}}{N_{\text{ref}}} \sqrt{\mathbb{E}_{p_{t|0}} [\|f(X_0) - \mathbb{E}_{p_{t|0}}[f(X_0)]\|^2]} \sqrt{\text{Tr} (\Sigma)}. \end{aligned}$$

Using Jensen inequality and (B.1) gives

$$\|\mathbb{E}_{p_{t|0}}[f(X_0)]\| \leq \mathbb{E}_{p_{t|0}}\|f(X_0)\| \leq c\mathbb{E}_{p_{t|0}}\|X_0 - \mu\|^2 = c\text{Tr}(\text{Cov}_{p_{t|0}}(X_0)) \leq \frac{cd}{\kappa(y)}.$$

On the other hand, since  $p_{t|0}$  is strongly log-concave (see Lemma B.1),  $\langle u, X - m \rangle$  are sub-Gaussian with variance proxy  $\kappa^{-1}$  for any unit vector  $u$  [56]. Standard moment estimates for sub-Gaussian distribution [57–59] then give

$$\mathbb{E}_{p_{t|0}}\|X_0 - \mu\|^4 \lesssim \frac{d^2}{\kappa^2},$$

thus

$$\mathbb{E}_{p_{t|0}}\|f(X_0)\|^2 \leq c^2\mathbb{E}_{p_{t|0}}\|X_0 - \mu\|^4 \lesssim \frac{c^2d^2}{\kappa^2}$$

Next using triangle inequality we have

$$\mathbb{E}_{p_{t|0}}\|f(X_0) - \mathbb{E}_{p_{t|0}}[f(X_0)]\|^2 \leq 2\mathbb{E}_{p_{t|0}}\|f(X_0)\|^2 + 2\|\mathbb{E}_{p_{t|0}}[f(X_0)]\|^2 \lesssim \frac{c^2d^2}{\kappa^2}.$$

We conclude

$$E \lesssim \frac{1}{1 - e^{-2t}} \frac{w_{\max}}{N_{\text{ref}}} \frac{cd}{\kappa} \sqrt{\text{Tr}(\Sigma)} \leq \frac{1}{1 - e^{-2t}} \frac{w_{\max}}{N_{\text{ref}}} \frac{cd^{3/2}}{\kappa^{3/2}}. \quad \square$$

## B.2. Proof of Proposition 3.2.

*Proof.* Substituting the exact Gaussian score  $s_0(x) = -\Sigma^{-1}(x - \mu_0)$  into the SNIS estimator in (3.10) and (3.7) yields

$$\hat{s}_{\text{CSE}} = -e^t \Sigma^{-1} [\hat{\mu}_{\text{SNIS}} - \mu_0], \quad \text{and } \hat{s}_{\text{TWD}} = -\frac{1}{1 - e^{-2t}} [y - e^{-t} \hat{\mu}_{\text{SNIS}}],$$

and all the assertions follows  $\square$

## B.3. Proof of Proposition 3.5.

*Proof.* By setting  $\frac{\partial J}{\partial \lambda} = 0$  we obtain

$$(B.4) \quad \lambda^* = \frac{\sigma_C^2 - \rho \sigma_T \sigma_C}{\sigma_T^2 + \sigma_C^2 - 2\rho \sigma_T \sigma_C}, \text{ and } J(\lambda^*) = \frac{\sigma_T^2 \sigma_C^2 (1 - \rho^2)}{\sigma_T^2 + \sigma_C^2 - 2\rho \sigma_T \sigma_C}.$$

Since  $\sigma_T^2 + \sigma_C^2 - 2\rho \sigma_T \sigma_C > 0$ , both assertions can be verified by direct algebraic manipulations.  $\square$

## Appendix C. Details of the local Gaussian score proxy.

This appendix records implementation details for the local Gaussian score proxies (DIAG and LR+D) and the optional  $k$ -mix recomputation step. These procedures are standard and are included only to make our experimental setup reproducible.

**C.1. Anchor fitting via weighted  $k$ NN.** Let  $X = \{x_0^i\}_{i=1}^{N_{\text{ref}}} \subset \mathbb{R}^d$  be reference samples from  $p_0$ . For each anchor  $x_0^i$ , we let  $\mathcal{N}_k(i)$  denote the indices of its  $k$  nearest neighbors in  $X$  under the ambient Euclidean metric. We set an adaptive bandwidth by

$$h_i^2 := \max_{j \in \mathcal{N}_k(i)} \|x_0^i - x_0^j\|_2^2.$$

We define unnormalized kernel weights  $\bar{w}_{ij}$  and their normalized versions  $w_{ij}$  by

$$\bar{w}_{ij} := \exp\left(-\frac{\|x_0^i - x_0^j\|_2^2}{2h_i^2}\right), \quad w_{ij} := \frac{\bar{w}_{ij}}{\sum_{\ell \in \mathcal{N}_k(i)} \bar{w}_{i\ell}}, \quad j \in \mathcal{N}_k(i).$$

We then compute the locally weighted mean

$$\mu_i := \sum_{j \in \mathcal{N}_k(i)} w_{ij} x_0^j.$$

Given a positive definite covariance model  $\Sigma_i \succ 0$ , the Gaussian score proxy at the anchor is  $\Sigma_i^{-1}(\mu_i - x_0^i)$ , as defined in (3.19) and (3.20).

---

**Algorithm C.1** Local Gaussian proxy at anchors (DIAG or LR+D)

---

- 1: **Input:**  $X = \{x_0^i\}_{i=1}^{N_{\text{ref}}} \subset \mathbb{R}^d$ , neighbor count  $k$ , ridge/noise-floor parameters, and (for LR+D) a rank  $r$ .
- 2: **for**  $i = 1, \dots, N_{\text{ref}}$  **do**
- 3:     Find  $\mathcal{N}_k(i)$  (the  $k$  nearest neighbors of  $x_0^i$  in  $X$ ).
- 4:     Set  $h_i^2 \leftarrow \max_{j \in \mathcal{N}_k(i)} \|x_0^i - x_0^j\|_2^2$ .
- 5:     Set  $\bar{w}_{ij} \leftarrow \exp(-\|x_0^i - x_0^j\|_2^2 / (2h_i^2))$  for  $j \in \mathcal{N}_k(i)$ .
- 6:     Normalize  $w_{ij} \leftarrow \bar{w}_{ij} / \sum_{\ell \in \mathcal{N}_k(i)} \bar{w}_{i\ell}$ .
- 7:     Compute  $\mu_i \leftarrow \sum_{j \in \mathcal{N}_k(i)} w_{ij} x_0^j$ .
- 8:     **If** mode=DIAG, construct  $\Sigma_i^{\text{DIAG}}$  as in §C.2.1.
- 9:     **If** mode=LR+D, construct  $\Sigma_i^{\text{LR+D}}$  as in §C.2.2.
- 10:    Store  $(\mu_i, \Sigma_i)$  and the anchor score  $\hat{s}_0(x_0^i) = \Sigma_i^{-1}(\mu_i - x_0^i)$ .
- 11: **end for**
- 12: **Output:**  $\{(\mu_i, \Sigma_i)\}_{i=1}^{N_{\text{ref}}}$  and  $\{\hat{s}_0(x_0^i)\}_{i=1}^{N_{\text{ref}}}$ .

---

## C.2. Covariance models and hyperparameters.

**C.2.1. Diagonal proxy (Diag).** For the diagonal proxy, we estimate per-coordinate variances from the weighted neighbor cloud and add an isotropic ridge (noise floor) to stabilize inversion. For  $\ell = 1, \dots, d$ , we define

$$v_{i,\ell} := \sum_{j \in \mathcal{N}_k(i)} w_{ij} (x_0^j(\ell) - \mu_i(\ell))^2, \quad \tau_i := \gamma \cdot \frac{1}{d} \sum_{\ell=1}^d v_{i,\ell},$$

where  $\gamma > 0$  is a dimensionless ridge multiplier. We then set

$$\Sigma_i^{\text{DIAG}} := \text{diag}(v_{i,1} + \tau_i, \dots, v_{i,d} + \tau_i).$$

The corresponding proxy score is defined in (3.19).

**C.2.2. Low-rank plus diagonal tail proxy (LR+D).** For the LR+D proxy, we estimate a rank- $r$  principal subspace from the weighted neighbors and represent the remaining energy by a diagonal tail. We let  $M_i \in \mathbb{R}^{k \times d}$  be the weighted residual matrix with rows

$$(M_i)_{(j,\cdot)} := \sqrt{w_{ij}} (x_0^j - \mu_i)^\top, \quad j \in \mathcal{N}_k(i).$$

---

**Algorithm C.2** Recompute ( $k$ -mix) mixture score at query  $x$ 


---

- 1: **Input:** query  $x$ , anchor parameters  $\{(\mu_i, \Sigma_i)\}_{i=1}^{N_{\text{ref}}}$ , and  $k_{\text{mix}}$ .
- 2: Find indices of the  $k_{\text{mix}}$  nearest anchors to  $x$ :  $\{i_m\}_{m=1}^M$ .
- 3: **for**  $m = 1, \dots, M$  **do**
- 4:     Compute
- 5:      $\ell_m \leftarrow \log \pi_m - \frac{1}{2}(x - \mu_{i_m})^\top \Sigma_{i_m}^{-1}(x - \mu_{i_m}) - \frac{1}{2} \log \det(2\pi \Sigma_{i_m})$ .
- 6: **end for**
- 7: Let  $a \leftarrow \max_m \ell_m$ , and set

$$\tilde{w}_m \leftarrow \exp(\ell_m - a) \Big/ \sum_{j=1}^M \exp(\ell_j - a).$$

- 7: **Return**  $\hat{s}_0^{\text{recomp}}(x) \leftarrow \sum_{m=1}^M \tilde{w}_m \Sigma_{i_m}^{-1}(\mu_{i_m} - x)$ .

---

We compute a rank- $r$  truncated SVD of  $M_i^\top M_i$  to obtain  $V_i \in \mathbb{R}^{d \times r}$  and  $\Lambda_i = \text{diag}(\lambda_{i,1}, \dots, \lambda_{i,r})$ . We let  $\tau_{i,\ell} > 0$  be a per-coordinate tail variance (with optional clipping from below to enforce a noise floor). We then set

$$\Sigma_i^{\text{LR+D}} := V_i \Lambda_i V_i^\top + \text{diag}(\tau_{i,1}, \dots, \tau_{i,d}).$$

The corresponding proxy score is defined in (3.20).

**Woodbury inversion.** For implementation, we write  $D_i := \text{diag}(\tau_{i,1}, \dots, \tau_{i,d})$  and apply the inverse using Woodbury to avoid forming dense  $d \times d$  matrices:

$$(D_i + V_i \Lambda_i V_i^\top)^{-1} = D_i^{-1} - D_i^{-1} V_i \left( \Lambda_i^{-1} + V_i^\top D_i^{-1} V_i \right)^{-1} V_i^\top D_i^{-1}.$$

**C.3.  $k$ -mix recomputation at query points.** A single local Gaussian can be biased in regions of high curvature or near crossings. To reduce this bias, we optionally recompute the proxy score at a query point  $x$  by treating the neighborhood as a compact Gaussian mixture.

We select indices  $\{i_m\}_{m=1}^M$  as the  $k_{\text{mix}}$  nearest anchors to  $x$ , where  $M := k_{\text{mix}} \ll N_{\text{ref}}$ . Using the stored anchor parameters  $\{(\mu_i, \Sigma_i)\}_{i=1}^{N_{\text{ref}}}$ , we form

$$q(x) := \sum_{m=1}^M \pi_m \mathcal{N}(x | \mu_{i_m}, \Sigma_{i_m}),$$

where  $\pi_m$  are simple priors (for example, proximity weights normalized to sum to one). The mixture score is

(C.1)

$$\nabla_x \log q(x) = \sum_{m=1}^M \tilde{w}_m(x) \Sigma_{i_m}^{-1}(\mu_{i_m} - x), \quad \tilde{w}_m(x) := \frac{\pi_m \mathcal{N}(x | \mu_{i_m}, \Sigma_{i_m})}{\sum_{j=1}^M \pi_j \mathcal{N}(x | \mu_{i_j}, \Sigma_{i_j})}.$$

We evaluate  $\tilde{w}_m(x)$  using a log-sum-exp computation for numerical stability.

*Remark* The  $k$ -mix recomputation accepts either **DIAG** or **LR+D** anchors (see [subsection 3.5](#)). Even with diagonal anchors, recomputation mitigates single-Gaussian bias in high-curvature regions, while remaining  $O(k_{\text{mix}}d)$  per query.

**C.4. Computational complexity.** The costs separate into an offline anchor-fit phase and an online query phase.

**Neighbor search.** If one computes all  $k$ NN sets  $\{\mathcal{N}_k(i)\}$  by brute force, the cost is  $O(N_{\text{ref}}^2 d)$  time and  $O(N_{\text{ref}} d)$  storage for the data. In low ambient dimension, tree-based methods can reduce this cost, and in higher dimension approximate  $k$ NN can be used. Since preprocessing is independent of diffusion time, it is amortized across all subsequent score evaluations.

**Per-anchor fitting.** For  $\text{DIAG}$ , computing local moments costs  $O(kd)$  time and  $O(d)$  memory per anchor, and applying  $(\Sigma_i^{\text{DIAG}})^{-1}$  is elementwise. For  $\text{LR+D}$ , estimating the rank- $r$  subspace costs  $O(kdr)$  time (or  $O(kd \min\{d, k\})$  with a dense SVD), and storing  $V_i$  costs  $O(dr)$  memory per anchor.

**Query-time evaluation.** If one uses the anchor-only proxy at an anchor location, no additional cost is incurred beyond applying  $\Sigma_i^{-1}$ . For recompilation at a general query  $x$ , the cost is dominated by evaluating  $M = k_{\text{mix}}$  components and normalizing mixture weights. With diagonal anchors this step is  $O(k_{\text{mix}}d)$  time. With  $\text{LR+D}$  anchors, applying the Woodbury inverse yields an effective cost  $O(k_{\text{mix}}dr)$  when  $r \ll d$ , plus  $O(k_{\text{mix}}d)$  for diagonal parts.

**C.5. Asymptotic remarks.** Under standard smoothness and positivity assumptions and classical  $k$ NN bandwidth scaling ( $k \rightarrow \infty$  and  $k/N_{\text{ref}} \rightarrow 0$ ), the single-component local Gaussian proxy is a consistent estimator of  $s_0(x)$ . Standard nonparametric analysis [49–51] yields

$$\left( \mathbb{E}_{p_0} \|\hat{s}_0(x) - s_0(x)\|_2^2 \right)^{1/2} = \mathcal{O}(N_{\text{ref}}^{-\frac{2}{d+4}}) \quad \text{for} \quad k \asymp N_{\text{ref}}^{\frac{4}{d+4}}, \text{<sup>2</sup>}$$

up to curvature-dependent constants and the chosen covariance structure. The  $\text{LR+D}$  choice (subsection 3.5) reduces bias in anisotropic neighborhoods, and the  $k$ -mix recompilation further mitigates single-mode bias in regions where mixture components have non-negligible overlap by recovering the mixture score (C.1). Because  $\|\hat{s}_0 - s_0\|_2 \rightarrow 0$  as  $N_{\text{ref}} \rightarrow \infty$  (provided  $k/N_{\text{ref}} \rightarrow 0$  [50]), the CSE term built from  $\hat{s}_0$  remains consistent at small diffusion times, and the blended score estimator  $\hat{s}_{\text{BLEND}}$  (3.17) inherits the ground-truth score behavior in the limit  $N_{\text{ref}} \rightarrow \infty$ .

## Appendix D. Parametric Distillation via a Critic-and-Gate Network.

In the main text, we developed a nonparametric, variance-optimal blended score estimator  $\hat{s}_{\text{BLEND}}$  (3.17)  $\hat{s}_{\text{BLEND}}(y, t)$  that combines the CSE and Tweedie identities. To facilitate deployment without a reference set at test time, we now provide a *parametric distillation* strategy that amortizes this blended score estimator  $\hat{s}_{\text{BLEND}}$  (3.17) into a single neural score model. This appendix outlines the minimal ingredients: the problem setup, a learning objective derived from a variance decomposition, and the theoretical justification for the training procedure.

**D.1. Setup and Learning Objective.** We begin by defining the forward dynamics. Let  $x_0 \sim p_0$ ,  $\xi \sim \mathcal{N}(0, I)$ , and for the Ornstein–Uhlenbeck process, let us define  $y = e^{-t}x_0 + \sigma_t \xi$  with  $\sigma_t^2 = 1 - e^{-2t}$ . We denote the per-particle signals defined in Sections 3.2–3.3 as follows:

$$a(x_0, t) = e^t s_0(x_0), \quad b(x_0, y, t) = -\sigma_t^{-2} (y - e^{-t}x_0).$$

We introduce a **gate** network  $g(y, t; \psi) \in [0, 1]$  which produces a blended per-particle signal defined by

$$z_g(x_0; y, t) = (1 - g(y, t; \psi)) a(x_0, t) + g(y, t; \psi) b(x_0, y, t).$$

---

<sup>2</sup>We use  $a_N \asymp b_N$  to denote that  $a_N$  and  $b_N$  are of the same asymptotic order.

Additionally, a **critic** network  $q(y, t; \omega)$  is introduced to predict the final score as a function of  $(y, t)$  alone. We train the parameters  $(\psi, \omega)$  by minimizing the population mean squared error (MSE):

$$(D.1) \quad \mathcal{L}(\psi, \omega) = \mathbb{E}_{x_0, \xi, t} \left[ \| z_g(x_0; y, t) - q(y, t; \omega) \|_2^2 \right].$$

**D.2. Variance Decomposition Analysis.** To understand the efficacy of this objective, we analyze it by conditioning on a fixed time-location  $(y, t)$ . Let  $\pi(\cdot | y, t)$  denote the posterior distribution of  $x_0$  given  $(y, t)$ . Abbreviating  $z_g = z_g(x_0; y, t)$  and  $q = q(y, t; \omega)$ , the law of total variance yields the pointwise decomposition

$$(D.2) \quad \mathbb{E}[\| z_g - q \|_2^2 | y, t] = \text{Var}_\pi(z_g) + \left\| \mathbb{E}_\pi[z_g] - q \right\|_2^2.$$

Taking the total expectation over  $(y, t)$  reveals that minimizing (D.1) enforces two complementary roles simultaneously.

First, regarding the critic, for any fixed gate configuration  $g$ , the inner minimum of (D.2) is attained when

$$q(y, t) = \mathbb{E}_\pi[z_g(x_0; y, t)].$$

In other words, the critic learns the *MSE-optimal* blended score at  $(y, t)$  corresponding to the current gate mixture.

Second, substituting this optimal  $q$  back into (D.2) leaves the gate with the objective to minimize  $\text{Var}_\pi(z_g)$ . Consequently,  $g$  is driven to find the *variance-minimizing* blend coefficient at each  $(y, t)$ , matching the optimal  $\lambda^*$  derived in the nonparametric setting.

**D.3. Relation to the Nonparametric Estimator.** This formulation mirrors the nonparametric approach derived in the main text. If we let  $a = s_{\text{CSE}}$  and  $b = s_{\text{TWD}}$ , the variance of the scalar blend  $z_\lambda = (1 - \lambda)a + \lambda b$  is minimized by

$$\lambda^* = \frac{\text{Var}[a] - \text{Cov}[a, b]}{\text{Var}[a] + \text{Var}[b] - 2\text{Cov}[a, b]},$$

where the moments are computed under  $\pi(\cdot | y, t)$ . The nonparametric SNIS plugin estimator approximates this  $\lambda^*(y, t)$  using posterior samples. As shown by the decomposition in (D.2), the parametric critic-and-gate architecture reproduces this exact population objective: the learned  $g(y, t; \psi)$  amortizes the calculation of  $\lambda^*(y, t)$ , while  $q(y, t; \omega)$  amortizes the resulting blended score, yielding a direct parametric distillation of the nonparametric rule.

**D.4. Proof-of-Concept Experiment (48-D GMM).** As a proof of concept for the functionality of critic gate score distillation, we evaluate a neural distillation of tweedies identity( baseline Denoising score matchibg) versus a critic gate distilled score network. We test on a dimension  $d=48$  Gaussian mixture with strongly curved, filamentary structure, using a 10-step reverse-OU sampler. The Critic Gate score network is trained using diagonal covariance proxy scores(3.5) learned from data alone. Figure D.1 shows qualitative projections: the distilled critic preserves filament geometry more closely than a DSM baseline. Table D.1 lists quantitative metrics at 15 steps; our critic gate score distillation outperforms the DSM baselines across all divergence metrics.

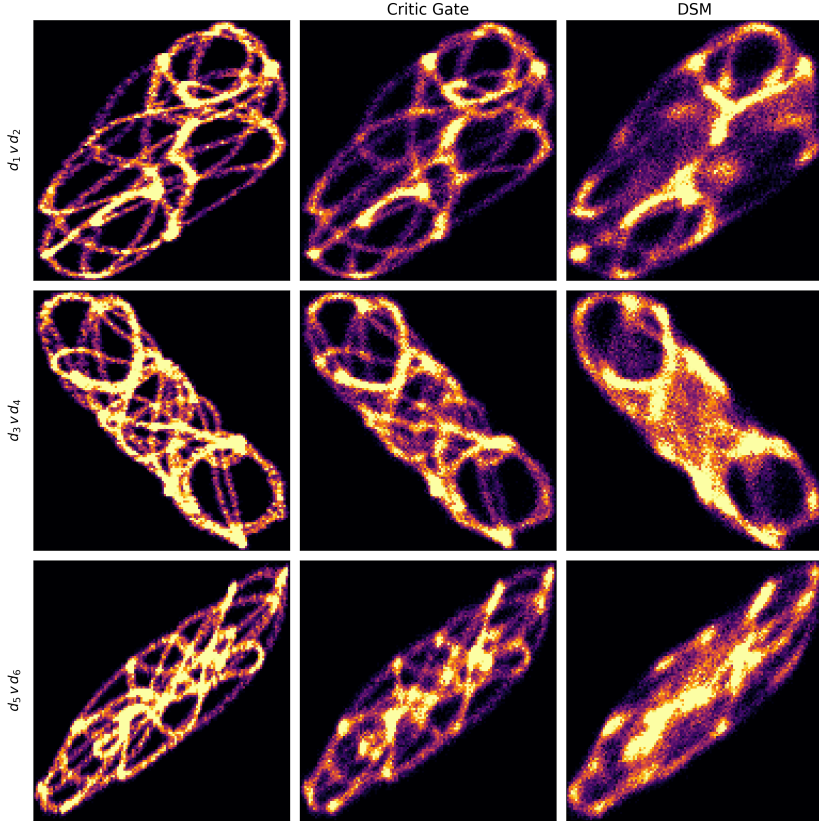


FIG. D.1. *Critic-and-Gate distillation on 48-D GMM (10 steps).* Qualitative density projections: left column (truth), middle (Critic-Gate), right (DSM). The distilled critic, trained by (D.1), recovers thin filamentary sets that DSM blurs.

TABLE D.1

*Quantitative comparison at 15 steps.* Metrics on matched samples. Arrows indicate the preferred direction:  $\downarrow$  means lower values are better (all metrics reported here are minimized).

Metric	DSM	Critic-Gate (ours)	Floor
MMD@15 $\downarrow$	0.03732	0.02507	0.02053
W2@15 $\downarrow$	0.05586	0.03865	0.02515
KSD@15 $\downarrow$	472.7	104.4	15.90

## Appendix E. Supplementary Results.

This appendix collects additional plots and experiments deferred from the main text. Unless stated otherwise, we use the same reverse-time discretization, diagnostic metrics, and evaluation protocol as in the main numerical section; full experimental details are deferred to [section F](#).

**E.1. Correlation across time and variance/bias profiles.** Our theory predicts that the Monte Carlo errors of the CSE and Tweedie estimators are negatively correlated (cf. [subsection 3.4.2](#)). We verify this empirically on the **6D helix GMM** in [Figure E.1](#) by plotting the correlation of the estimator errors as a function of diffusion time  $t$ :

$$\varepsilon_T(y, t) := \hat{s}_{\text{TWD}}(y, t) - s(y, t), \quad \varepsilon_C(y, t) := \hat{s}_{\text{CSE}}(y, t) - s(y, t),$$

$$\rho(t) = \frac{\mathbb{E}_{y \sim p_t} [\langle \varepsilon_T(y, t), \varepsilon_C(y, t) \rangle]}{\sqrt{\mathbb{E}_{y \sim p_t} \|\varepsilon_T(y, t)\|^2} \sqrt{\mathbb{E}_{y \sim p_t} \|\varepsilon_C(y, t)\|^2}}.$$

We estimate  $\rho(t)$  by Monte Carlo over  $y \sim p_t$ . The *ground-truth* curve evaluates the estimators using the exact  $s_0$  (and uses the true  $s(y, t)$  for error evaluation), while the *proxy* curve replaces  $s_0$  by the learned **diagonal** local-Gaussian proxy  $\hat{s}_0$  from [subsection 3.5](#) (still comparing to the true  $s(y, t)$ ). We drop time points with low importance-sampling quality using the ESS filter from [Footnote 1](#). As shown in [Figure E.1](#),  $\rho(t)$  is distinctly negative over a broad range of  $t$ , with a pronounced minimum near  $t \approx 10^{-3}$ , consistent with the small-time anti-correlation predicted in [subsection 3.4.2](#) and sufficient to yield variance cancellation in the blended estimator. This negative correlation between the estimator errors is preserved when using diagonal proxy score fit to data, all be it weaker especially for larger  $t$ .

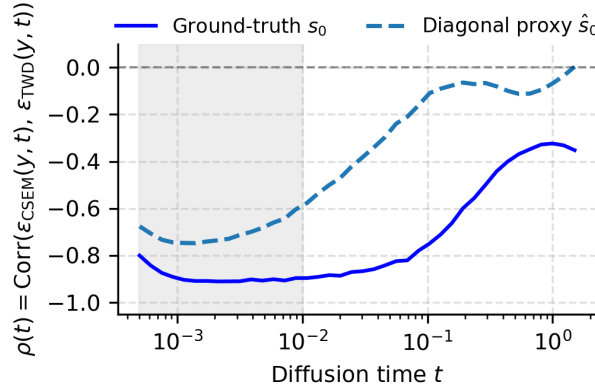


FIG. E.1. *Anti-correlation between CSE estimator (3.10) and Tweedie estimator (3.7) on the 6D helix GMM.* The grey region highlights the regime where anti-correlation is strongest (near  $t \approx 10^{-3}$ ). The diagonal-proxy curve (dashed; *DIAG* from [subsection 3.5](#)) preserves the negative-correlation effect that underlies variance reduction in the blended estimator (3.13).

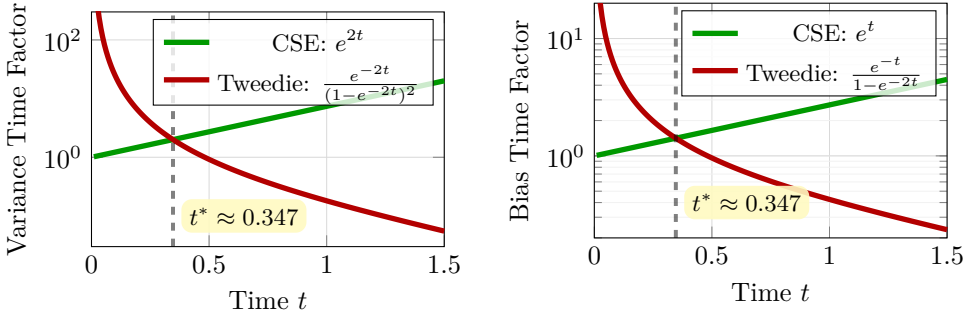


FIG. E.2. *Relative variance and bias (due to SNIS) of the Tweedie and CSE non-parametric score estimators as a function of time  $t$ . The former has low variance/bias at large  $t$  but diverges at  $t = 0$ , while the latter has low variance/bias at small  $t$  but grows exponentially. For both bias and variances, the crossover occurs at the same point as for variance:  $t^* = \ln(2)/2 \approx 0.347$ .*

**E.2. Posterior sampling results.** We provide additional posterior sampling diagnostics for synthetic and image inverse problems.

**12D GMM with rank-1 likelihood.** We consider a 12D Gaussian mixture prior constrained by a rank-1 Gaussian likelihood, and visualize samples in PCA planes fitted to posterior reference samples (see [section F](#) for exact construction). [Figure E.3](#) compares the Tweedie baseline with blended variants.

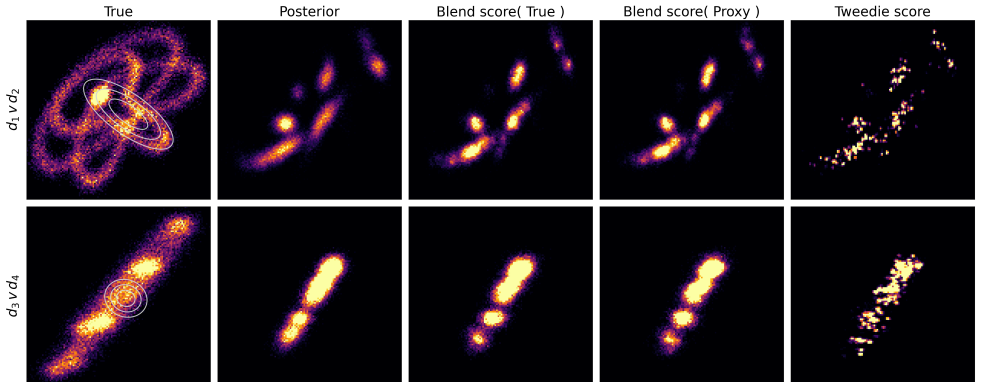


FIG. E.3. *Posterior sampling (12D,  $N=1600$ ). Projected histograms in PCA planes ( $d_1, d_2$ ), ( $d_2, d_5$ ) (principal directions fitted to the posterior via importance-weighted prior samples). Blend (true) uses the exact target score; Blend (proxy) uses the LR+D local Gaussian score proxy from [subsection 3.5](#) fit to the raw data; Tweedie is the baseline. White contours indicate likelihood level sets. Both blends capture the localized posterior manifold, while Tweedie yields fragmented samples because it misses local features.*

In this example, *Blend (true)* and *Blend (proxy)* both approximate the posterior ridge and spread well, while Tweedie tends to fragment/collapse onto a small set of high-weight reference particles near the posterior concentration.

**MNIST deblurring panel.** We include multi-panel posterior sample summaries in [Figure E.4](#). These visualize individual posterior samples from the MNIST deblurring problem for all relevant samplers.

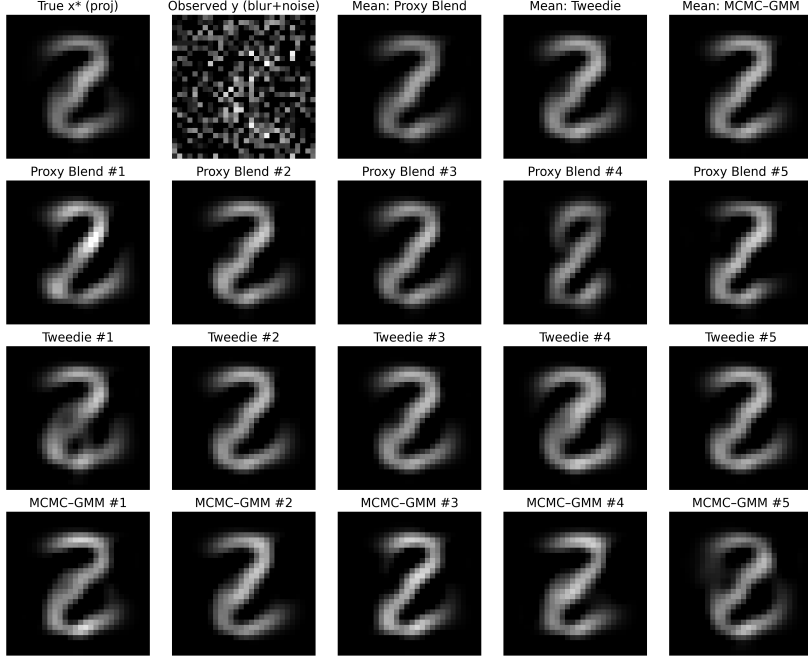


FIG. E.4. *MNIST deblurring (N=18,000 references)*. Visual comparison: Blend (Proxy) produces sharper posterior means and more coherent individual samples than Tweedie only. Samples align with IS contours (cyan; HPD mass levels 0.4 to 0.999). All samplers use the Heun PC (second order) integrator.

All samplers produce visually reasonable posterior samples in this run, with *Blend (Proxy)* showing the fewest visible artifacts among the displayed panels. All samplers produce visually reasonable posterior samples in this run, with *Blend (Proxy)* showing the fewest visible artifacts among the displayed panels.

**Inverse heat equation.** We report a linear PDE inverse problem in the same posterior-sampling framework used for Navier–Stokes (subsection 4.3.1), with identical diagnostics and reverse-time integration; only the forward model differs. Specifically, we infer a log-conductivity field  $u(x)$  from sparse point observations of the temperature field  $\omega(x)$  on  $\Omega = (0, 1)^2$ :

$$-\nabla \cdot (e^{u(x)} \nabla \omega(x)) = 20, \quad \omega = 0 \text{ on } \Gamma_{\text{ext}}, \quad n \cdot (e^{u(x)} \nabla \omega(x)) = 0 \text{ on } \Gamma_{\text{root}}.$$

$$u(x; \alpha) = \sum_{i=1}^q \sqrt{\lambda_i} \phi_i(x) \alpha_i, \quad \alpha \in \mathbb{R}^q, \quad q = 15,$$

$$p_0(\alpha) = \mathcal{N}(0, I), \quad s_0(\alpha) := \nabla_\alpha \log p_0(\alpha) = -\alpha,$$

$$\mathcal{L}(\alpha) := p(y \mid \alpha) = \mathcal{N}(y; F(\alpha), \sigma_{\text{obs}}^2 I), \quad \nabla_\alpha \log \mathcal{L}(\alpha) = \frac{1}{\sigma_{\text{obs}}^2} J_F(\alpha)^\top (y - F(\alpha)).$$

Representative PCA-plane histograms of posterior samples are shown in Figure E.6, and reconstructed fields are shown in Figure E.5. Following the Navier–Stokes table format, we summarize quantitative diagnostics in Table E.1.

TABLE E.1

**Inverse heat quantitative results.** Same metrics and diagnostics as in the Navier–Stokes study (Table 4.1). Arrows indicate the preferred direction:  $\downarrow$  means lower values are better (all metrics reported here are minimized), with MALA serving as the reference for  $MMD \rightarrow MALA$ .

Method	$MMD \rightarrow MALA \downarrow$	$RMSE_\alpha \downarrow$	$RMSE_{amb} \downarrow$	<b>Fwd Err</b> $\downarrow$	<b>KSD</b> $\downarrow$	$\widetilde{KL} \downarrow$
Tweedie ( $\hat{s}_{TWD}$ )	0.145	0.470	0.111	0.107	16.0	111.2
Blend Posterior ( $\hat{s}_{BLEND}$ )	0.088	0.465	0.106	0.101	1.008	58.4
MALA (Reference)	0.000	0.457	0.101	0.096	0.883	43.1

Visually, *Blend Posterior* matches the MALA reference more closely in the PCA marginals, and this improved agreement is reflected consistently across the reported diagnostics and in field reconstruction plot ; Tweedie exhibits the same kind of fragmentation/collapse seen in the synthetic posterior histograms.

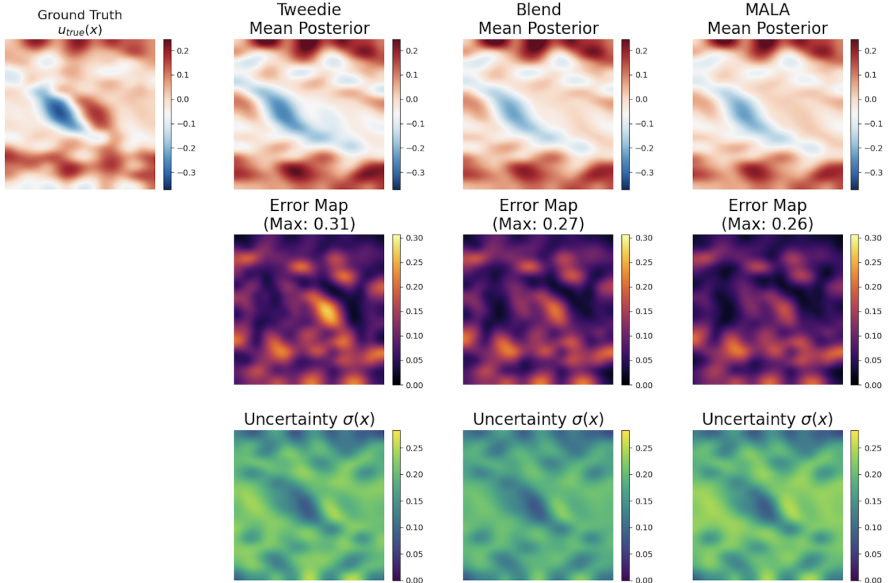
Inverse Heat Equation ( $k=15$ ): Posterior Field Reconstruction

FIG. E.5. *Inverse heat-conductivity posterior reconstruction (KL dim.  $k=15$ )*. The conductivity parameter field  $u(x)$  is reconstructed on a  $16 \times 16$  grid from posterior samples in the reduced KL coefficient space.

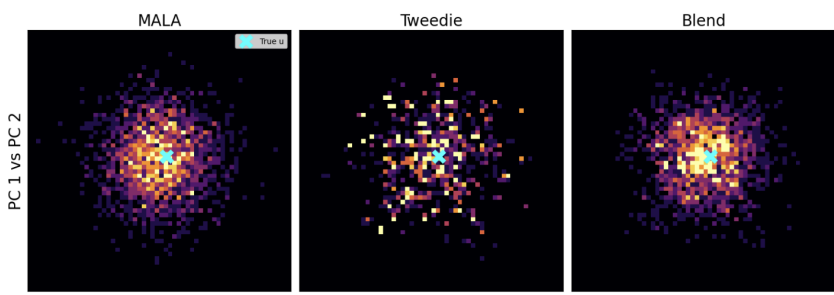


FIG. E.6. *Histograms of posterior samples projected onto the first two principal components (PCA) of the target distribution. The Blend Posterior (orange) captures the mode and variance of the reference distribution significantly better than the standard Tweedie approximation (blue), closely matching the MALA baseline.*

**Appendix F. Reproducibility.** This appendix summarizes implementation details and provides a checklist of all experiment hyperparameters needed to reproduce the figures and tables in the main text.

**F.1. OU corruption, time grid, and reverse-time integration. Forward OU process.** We use the Ornstein–Uhlenbeck (OU) forward dynamics

$$dX_t = -X_t dt + \sqrt{2} dW_t, \quad X_0 \sim p_0,$$

so that

$$X_t \mid X_0 = x \sim \mathcal{N}(e^{-t}x, \sigma_t^2 I), \quad \sigma_t^2 := 1 - e^{-2t}.$$

**Reverse-time sampler.** Given a score estimator  $\hat{s}(y, t) \approx \nabla_y \log p_t(y)$ , we integrate the reverse-time SDE. We always use the same integrator for Tweedie, CSE, and Blend and across all experiments to ensure comparability:

$$dY_t = (Y_t + 2\hat{s}(Y_t, t)) dt + \sqrt{2} d\bar{W}_t,$$

from  $t_{\max}$  down to  $t_{\min}$ , initialized at  $Y_{t_{\max}} \sim \mathcal{N}(0, I)$ .

**Time grid.** For all experiments we use a log-spaced grid  $t_K = t_{\max} > \dots > t_0 = t_{\min}$  with  $t_{\min} = 5 \times 10^{-4}$  and  $t_{\max} = 1.5$ .

**Heun predictor–corrector.** To step from  $t_{k+1}$  to  $t_k$  with  $\delta := t_{k+1} - t_k > 0$ , define the reverse drift  $f(y, t) := y + 2\hat{s}(y, t)$  and update

$$\text{Predictor: } \tilde{y}_k = y_{k+1} - \delta f(y_{k+1}, t_{k+1}) + \sqrt{2\delta} z,$$

$$\text{Corrector: } y_k = y_{k+1} - \frac{\delta}{2} \left( f(y_{k+1}, t_{k+1}) + f(\tilde{y}_k, t_k) \right) + \sqrt{2\delta} z,$$

where  $z \sim \mathcal{N}(0, I_d)$  is drawn once per step and shared between predictor and corrector. We report results as a function of *number of function evaluations* (NFE), counting each call to  $\hat{s}(\cdot, t)$ .

**F.2. SNIS details, median-of-means, and ESS filtering. SNIS for conditional expectations.** For any function  $\varphi$ , conditional expectations under  $p_{t|0}(x_0 \mid y)$  are estimated from a reference set  $\{x_0^{(i)}\}_{i=1}^{N_{\text{ref}}} \sim p_0$  via self-normalized importance sampling:

$$\mathbb{E}_{p_{t|0}(\cdot|y)}[\varphi(X_0)] \approx \sum_{i=1}^{N_{\text{ref}}} \tilde{w}_i(y, t) \varphi(x_0^{(i)}), \quad \tilde{w}_i = \frac{\exp(\ell_i - a)}{\sum_j \exp(\ell_j - a)},$$

where  $\ell_i$  are log-weights (computed in log space for stability) and  $a = \max_i \ell_i$  is the log-sum-exp shift. For prior sampling, the weights are proportional to the OU transition density  $p(y \mid x_0^{(i)})$ . For posterior sampling, we additionally *tilt* the log-weights by  $\log L(y_{\text{obs}} \mid x_0^{(i)})$ .

**Median-of-means (MoM).** To reduce sensitivity to heavy-tailed importance weights, we compute SNIS estimates over independent batches (each with its own reference sub-sample) and aggregate with a median-of-means rule. Record the number of batches  $B$  and the per-batch reference size  $N_{\text{ref}}^{(\text{batch})}$  used in each experiment.

**ESS thresholding.** We quantify importance-weight quality using the effective sample size

$$\text{ESS}(y, t) := \frac{1}{\sum_{i=1}^{N_{\text{ref}}} \tilde{w}_i(y, t)^2}.$$

Following Footnote 1 in the main text, time points with  $\text{ESS}(y, t) < \tau_{\text{ESS}}$  are discarded, and we use  $\tau_{\text{ESS}} = 0.05 N_{\text{ref}}$  in all experiments.

**F.3. Local score proxies for  $s_0$ .** When  $s_0(x) = \nabla_x \log p_0(x)$  is unavailable, we approximate it from the reference set using the local Gaussian proxies from Section 3.5:

1. For each anchor  $x_0^{(i)}$ , compute its  $k$  nearest neighbors  $N_k(i)$  in the reference set.
2. Compute a locally weighted mean  $\mu_i$  and a structured covariance estimate  $\Sigma_i$ .
3. Define the anchor score proxy  $\hat{s}_0(x_0^{(i)}) := \Sigma_i^{-1}(\mu_i - x_0^{(i)})$ .

We use two structured families for  $\Sigma_i$ :

- **Diag:**  $\Sigma_i$  is diagonal (per-coordinate variance with ridge stabilization).
- **LR+D:**  $\Sigma_i = V_i V_i^\top + D_i$  with rank  $r$  and diagonal  $D_i$  (Woodbury inverse at query time).

**Parameters to log (proxy).** Record:  $k$  (neighbor count),  $r$  (rank for LR+D), the ridge/diagonal floor used for stabilization, and whether the proxy is evaluated at anchors only or recomputed at general queries using a  $k_{\text{mix}}$ -mixture.

**MALA sampler.** Given a differentiable target density  $\pi(\alpha)$  on  $\mathbb{R}^q$  (e.g.,  $\pi(\alpha) \propto p_0(\alpha)L(\alpha)$  in white-box experiments, or an approximate  $\pi$  obtained by replacing  $p_0$  with a differentiable surrogate prior), the Metropolis-adjusted Langevin algorithm (MALA) uses the proposal

$$\alpha' = \alpha + \frac{h}{2} \nabla_\alpha \log \pi(\alpha) + \sqrt{h} z, \quad z \sim \mathcal{N}(0, I_q),$$

where  $h > 0$  is the stepsize. The proposal density is Gaussian,

$$q(\alpha' | \alpha) = \mathcal{N}\left(\alpha'; \alpha + \frac{h}{2} \nabla \log \pi(\alpha), h I_q\right).$$

We accept  $\alpha'$  with probability

$$a(\alpha, \alpha') = \min\left\{1, \frac{\pi(\alpha') q(\alpha | \alpha')}{\pi(\alpha) q(\alpha' | \alpha)}\right\},$$

and otherwise retain the current state. In our experiments we run MALA chains for 2,000 iterations with a burn-in of 500 steps; the retained post-burn-in states are treated as samples from the reference posterior.

**F.4. Metrics and evaluation protocols.** We provide exact definitions for metrics used in the body of the text.

**MMD.** Given samples  $X = \{x_i\}_{i=1}^n \sim P$  and  $Y = \{y_j\}_{j=1}^m \sim Q$ , the (biased) squared MMD is

$$\text{MMD}_k^2(P, Q) \approx \frac{1}{n^2} \sum_{i, i'} k(x_i, x_{i'}) + \frac{1}{m^2} \sum_{j, j'} k(y_j, y_{j'}) - \frac{2}{nm} \sum_{i, j} k(x_i, y_j).$$

We use RBF kernels  $k_\sigma(x, y) = \exp(-\|x - y\|^2/2\sigma^2)$  with a multiscale bandwidth grid  $\{\sigma_\ell\}_\ell$  obtained from the median heuristic (record multipliers and the subsample size used to estimate the median distance).

**KSD.** For a target score  $s(x) = \nabla_x \log \pi(x)$  and a positive definite kernel  $k$ , the squared Kernel Stein Discrepancy is  $\text{KSD}^2(Q, \pi) = \mathbb{E}_{x, x' \sim Q}[u_s(x, x')]$ , with the Stein kernel

$$u_s(x, x') = s(x)^\top k(x, x')s(x') + s(x)^\top \nabla_{x'} k(x, x') \\ + s(x')^\top \nabla_x k(x, x') + \text{tr}(\nabla_x \nabla_{x'} k(x, x')).$$

We use an inverse-multipquadric kernel  $k(x, y) = (c^2 + \|x - y\|^2)^\beta$  with fixed  $(c, \beta)$ ; record  $(c, \beta)$  and whether an unbiased U-statistic or V-statistic estimator is used.

**Score RMSE.** When ground-truth scores are available, we report

$$\text{RMSE}(\hat{s}) := \left( \frac{1}{|\mathcal{T}|} \sum_{t \in \mathcal{T}} \mathbb{E}_{y \sim p_t} [\|\hat{s}(y, t) - s(y, t)\|^2] \right)^{1/2},$$

estimated by Monte Carlo over  $y \sim p_t$  on the same  $t$ -grid.

**Sliced Wasserstein-2.** For distributions  $P, Q$  on  $\mathbb{R}^d$ , SW2 is estimated by averaging 1D Wasserstein-2 distances over random directions  $\theta \in \mathbb{S}^{d-1}$ . Given samples  $X = \{x_i\}_{i=1}^n \sim P$  and  $Y = \{y_j\}_{j=1}^m \sim Q$ , form the projected scalars  $u_i = \theta^\top x_i$  and  $v_j = \theta^\top y_j$ . Assuming  $n = m$  (or after subsampling the larger set to match the smaller), sort  $u_{(1)} \leq \dots \leq u_{(n)}$  and  $v_{(1)} \leq \dots \leq v_{(n)}$  and compute

$$\widehat{W}_2^2(\theta) := \frac{1}{n} \sum_{i=1}^n (u_{(i)} - v_{(i)})^2.$$

With  $L$  directions  $\{\theta_\ell\}_{\ell=1}^L$ , we report

$$\widehat{\text{SW2}}(P, Q) := \frac{1}{L} \sum_{\ell=1}^L \widehat{W}_2^2(\theta_\ell).$$

Record the number of projections  $L$  and whether antithetic pairing is used.

**MNIST image metrics.** Pixels are scaled to  $[0, 1]$ . For a reconstruction  $\hat{x}$  and ground truth  $x$ , we report

$$\text{PSNR}(\hat{x}, x) = 20 \log_{10} \left( \frac{1}{\sqrt{\text{MSE}(\hat{x}, x)}} \right).$$

**Coverage.** Coverage is the fraction of pixels whose ground-truth value lies inside the empirical 90% credible interval computed from posterior samples:

$$\text{Coverage}(x) = \frac{1}{d} \sum_{i=1}^d \mathbf{1} \left\{ x_i \in [Q_{0.05}(\{x_i^{(s)}\}), Q_{0.95}(\{x_i^{(s)}\})] \right\}.$$

We additionally report  $\mathbb{E}_{x \sim \pi}[\log p_{\text{KDE}}(x)]$  where  $p_{\text{KDE}}$  is a KDE fit to posterior samples; record the kernel family and bandwidth rule (including any scalar multipliers).

**Coefficient-space mean error (RMSE $_\alpha$ ).** Let  $\alpha_* \in \mathbb{R}^q$  denote the ground-truth reduced coordinates used to generate the synthetic observation (e.g., KL coefficients for Navier–Stokes, PCA coefficients for MNIST). Given posterior samples  $\{\alpha^{(s)}\}_{s=1}^S$ , define the posterior mean estimator

$$\bar{\alpha} := \frac{1}{S} \sum_{s=1}^S \alpha^{(s)}.$$

We report the coefficient-space mean error

$$\text{RMSE}_\alpha := \frac{\|\bar{\alpha} - \alpha_\star\|_2}{\sqrt{q}}.$$

**Ambient-space mean error** (RMSE<sub>amb</sub>). Let  $G : \mathbb{R}^q \rightarrow \mathbb{R}^d$  denote the deterministic map from reduced coordinates to the ambient object (field/image), e.g.

$$\begin{aligned} \text{Navier-Stokes: } G(\alpha) &= w_0(\cdot; \alpha) \text{ (discretized on the simulation grid),} \\ \text{MNIST: } G(\alpha) &= \mu + U\alpha \in \mathbb{R}^{784}. \end{aligned}$$

Define the ambient posterior mean estimator

$$\bar{x} := \frac{1}{S} \sum_{s=1}^S G(\alpha^{(s)}), \quad x_\star := G(\alpha_\star).$$

We report

$$\text{RMSE}_{\text{amb}} := \frac{\|\bar{x} - x_\star\|_2}{\sqrt{d}}.$$

**Forward/data-fit error** (Fwd Err). Let  $F$  denote the forward operator mapping reduced coordinates to the (noise-free) observation space, and define the noiseless observation

$$y_{\text{clean}} := F(\alpha_\star).$$

We report the forward relative error of the posterior mean,

$$\text{FwdErr} := \frac{\|F(\bar{\alpha}) - y_{\text{clean}}\|_2}{\|y_{\text{clean}}\|_2},$$

which measures how well the inferred posterior mean reproduces the forward map at the sensor/pixel level.

**KL-type diagnostic** ( $\widetilde{\text{KL}}$ ). In white-box settings where the unnormalized posterior density is available up to a normalizer,

$$p_{\text{post}}(\alpha | y) \propto p_0(\alpha) L(\alpha),$$

we report the unnormalized KL form (KL up to an additive constant shared across methods)

$$\widetilde{\text{KL}}(q) := -\widehat{H}(q) - \mathbb{E}_{\alpha \sim q} [\log p_0(\alpha) + \log L(\alpha)],$$

where  $\widehat{H}(q)$  is an entropy estimator for the sampler distribution  $q$  (we use a  $k$ NN entropy estimator), and the expectation is estimated by Monte Carlo over the generated samples:

$$\mathbb{E}_{\alpha \sim q} [\log p_0(\alpha) + \log L(\alpha)] \approx \frac{1}{S} \sum_{s=1}^S (\log p_0(\alpha^{(s)}) + \log L(\alpha^{(s)})).$$

For a fixed posterior (fixed data  $y$ ),  $\widetilde{\text{KL}}(q)$  differs from the true  $\text{KL}(q \| p_{\text{post}})$  only by an additive constant  $-\log Z(y)$ , and hence is comparable across methods on the same inverse problem instance.

**F.5. Experiment-specific hyperparameters.** The main text defers concrete numerical settings (e.g., helix parameterization, kernel bandwidth grids, and SNIS batch sizes) to this appendix. Below are the specific hyperparameters, model configurations, and sampling settings used to generate the results in Sections 4.1–4.6.

**Regime Sweep subsection 4.2.** **Model:** The prior is a Spectral GMM with  $K_{\text{mix}} = 64$  components. Means are drawn on a whitened sphere of radius  $R = 2.0$ , with covariance eigenvalues decaying as  $\lambda_i \propto i^{-2}$  ( $\alpha = 1$ , “Helix” geometry). The forward operator is diagonal,  $A = \text{diag}(i^{-1})$ . **Sweep Parameters:** We sweep dimensions  $d \in \{3, 6, 12, 24\}$  and relative noise levels  $\sigma_{\text{rel}} \in [0.025, 1.0]$  (24 log-spaced steps). Absolute noise is scaled as  $\sigma_{\text{abs}} = \sigma_{\text{rel}} \cdot \sqrt{\mathbb{E}\|Ax\|^2}$ . **Sampling:** Heun Predictor-Corrector integrator with  $K = 30$  steps. Time schedule is log-spaced from  $t_{\text{max}} = 2.5$  to  $t_{\text{min}} = 3 \times 10^{-4}$ . Importance weights use a fixed bank of  $N_{\text{ref}} = 2,000$  samples. **Metrics:** MMD uses a Gaussian kernel with  $\sigma = 0.5\sqrt{d/2}$ . KSD uses multiscale bandwidths  $\sigma \in \{0.1, \dots, 1.0\}$ .

**Navier–Stokes subsection 4.3.1.** **Model:** 2D Vorticity-Stream formulation on a  $32 \times 32$  grid with viscosity  $\nu = 10^{-3}$ . The latent variable is the initial vorticity  $\omega_0$ , parameterized by a KL expansion with  $d = 24$  ( $\mathcal{N}(0, I_{24})$  prior). **Observations:** Measurements are taken at final time  $T = 10$  at  $m = 100$  random spatial points. Noise level is  $\sigma_{\text{obs}} = 0.3$ . Likelihood gradients are computed via JAX adjoints. **Sampling:** Heun integrator with  $K = 50$  steps and schedule  $t \in [1.0, 10^{-3}]$ . The reference bank contains  $N_{\text{ref}} = 20,000$  samples (batch size 1,000).

**Heat equation Inverse section E .** **Model:** The domain is a 2D square discretized on a  $15 \times 15$  FEM grid (256 nodes). The latent parameter is the log-conductivity field, parameterized by a KL expansion with dimension  $d = 15$ . **Observations:** We observe the temperature field at  $m = 25$  randomly selected sensors with additive Gaussian noise  $\sigma_{\text{obs}} = 0.11$ . **Sampling:** We use the exact prior score for the conditional score model. The sampler runs for  $K = 50$  steps on a log-spaced schedule. The reference set size is  $N_{\text{ref}} = 20,000$ , processed in batches of size  $B = 4,096$ .

**MNIST Deblurring subsection E.2.** **Model:** The latent space is defined by a PCA projection ( $d = 15$ ) fitted on  $N = 50,000$  training images. The prior is modeled as a Gaussian Mixture Model (GMM) with  $K_{\text{mix}} = 512$  components, fitted via Expectation-Maximization (EM) on the latent training data. The forward model is a Gaussian blur with  $\sigma_{\text{blur}} = 2.6$  pixels and additive noise  $\sigma_{\text{obs}} = 0.3$ . **Sampling:** The proxy score is a Local PCA model with rank  $r = 12$ . The sampler runs for  $K = 20$  steps from  $t_{\text{max}} = 2.0$  to  $t_{\text{min}} = 5 \times 10^{-4}$ . **Validation:** We use  $N_{\text{ref}} = 18,000$  reference samples for importance sampling and metrics. The ground truth baseline is a MALA sampler running for 3,000 steps (after 3,000 warmup steps) with adaptive step size targeting an acceptance rate of  $\approx 0.57$ .

**F.6. Code Availability.** The source code, configuration scripts, and data generation utilities used to produce the results in this paper are available in the public GitHub repository:

[https://github.com/alduston/CSE\\_diff](https://github.com/alduston/CSE_diff)

The repository contains the exact Jupyter notebooks and Python scripts referenced in this reproducibility checklist, allowing for full replication of the regime sweeps, inverse problem solvers, and deblurring experiments.

## References.

- [1] Jonathan Ho, Ajay Jain, and Pieter Abbeel. Denoising diffusion probabilistic models. In *Advances in Neural Information Processing Systems (NeurIPS)*, 2020. URL <https://proceedings.neurips.cc/paper/2020/file/4c5bcfec8584af0d967f1ab10179ca4b-Paper.pdf>.
- [2] Yang Song, Jascha Sohl-Dickstein, Diederik P. Kingma, Abhishek Kumar, Stefano Ermon, and Ben Poole. Score-based generative modeling through stochastic differential equations. In *International Conference on Learning Representations (ICLR)*, 2021. URL <https://openreview.net/forum?id=PxTIG12RRHS>.
- [3] Prafulla Dhariwal and Alexander Quinn Nichol. Diffusion models beat GANs on image synthesis. In *Advances in Neural Information Processing Systems (NeurIPS)*, 2021. URL <https://proceedings.neurips.cc/paper/2021/file/49ad23d1ec9fa4bd8d77d02681df5cfa-Paper.pdf>.
- [4] Yaron Lipman, Ricky T. Q. Chen, Heli Ben-Hamu, Maximilian Nickel, and Matt Le. Flow matching for generative modeling, 2022. URL <https://arxiv.org/abs/2210.02747>. NeurIPS 2023 (poster).
- [5] Xingchao Liu, Chengyue Gong, and Qiang Liu. Flow straight and fast: Learning to generate and transfer data with rectified flow. In *International Conference on Learning Representations (ICLR)*, 2023. URL <https://arxiv.org/abs/2209.03003>.
- [6] Yang Song, Prafulla Dhariwal, Mark Chen, and Ilya Sutskever. Consistency models. In *Proceedings of the 40th International Conference on Machine Learning (ICML)*, 2023. URL <https://arxiv.org/abs/2303.01469>.
- [7] Tero Karras, Miika Aittala, Timo Aila, and Samuli Laine. Elucidating the design space of diffusion-based generative models. In *Advances in Neural Information Processing Systems (NeurIPS)*, 2022.
- [8] Alex Nichol and Prafulla Dhariwal. Improved denoising diffusion probabilistic models. In *International Conference on Machine Learning (ICML)*, pages 8162–8171. PMLR, 2021.
- [9] Jiaming Song, Chenlin Meng, and Stefano Ermon. Denoising diffusion implicit models. In *International Conference on Learning Representations (ICLR)*, 2021.
- [10] Cheng Lu, Yuhao Zhou, Fan Bao, Jianfei Chen, Chongxuan Li, and Jun Zhu. Dpm-solver: A fast ode solver for diffusion probabilistic model sampling in around 10 steps. In *Advances in Neural Information Processing Systems (NeurIPS)*, 2022.
- [11] Jonathan Ho, Ajay Jain, and Pieter Abbeel. Denoising diffusion probabilistic models. In *Advances in Neural Information Processing Systems*, volume 33, pages 6840–6851, 2020.
- [12] Xingchao Liu, Chengyue Gong, and Qiang Liu. Flow straight and fast: Learning to generate and transfer data with rectified flow. *arXiv preprint arXiv:2209.03003*, 2022.
- [13] Chieh-Hsin Lai, Yuhta Takida, Naoki Murata, Toshimitsu Uesaka, Yuki Mitsu-fuji, and Stefano Ermon. FP-Diffusion: Improving score-based diffusion models by enforcing the underlying score fokker–planck equation. In *International Conference on Machine Learning (ICML)*. PMLR, 2023.
- [14] Zheyuan Hu, Zhongqiang Zhang, George Em Karniadakis, and Kenji Kawaguchi. Score-based physics-informed neural networks for high-dimensional fokker–planck equations. *arXiv preprint arXiv:2402.07465*, 2024.
- [15] Mo Zhou, Stanley Osher, and Wuchen Li. Simulating fokker–planck equations via mean field control of score-based normalizing flows. *arXiv preprint arXiv:2506.05723*, 2025.

- [16] Aapo Hyvärinen. Estimation of non-normalized statistical models by score matching. *Journal of Machine Learning Research*, 6:695–709, 2005.
- [17] Bharath K Sriperumbudur, Kenji Fukumizu, Arthur Gretton, Aapo Hyvärinen, and Revant Kumar. Density estimation in infinite dimensional exponential families. *Journal of Machine Learning Research*, 18(57):1–59, 2017.
- [18] Michael Arbel and Arthur Gretton. Kernel conditional exponential family. In *Proceedings of the 21st International Conference on Artificial Intelligence and Statistics (AISTATS)*, volume 84 of *Proceedings of Machine Learning Research*, pages 1337–1346. PMLR, 2018.
- [19] Li K. Wenliang, Danica J. Sutherland, Heiko Strathmann, and Arthur Gretton. Learning deep kernels for exponential family densities. In *International Conference on Machine Learning (ICML)*, volume 97 of *Proceedings of Machine Learning Research*, pages 6737–6746. PMLR, 2019.
- [20] Yuhao Zhou, Jiaxin Shi, and Jun Zhu. Nonparametric score estimators. In *International Conference on Machine Learning (ICML)*, volume 119 of *Proceedings of Machine Learning Research*, pages 11513–11523. PMLR, 2020.
- [21] Q. Liu and D. Wang. Stein variational gradient descent, 2016. PLACEHOLDER.
- [22] Qiang Liu, Jason Lee, and Michael Jordan. A kernelized stein discrepancy for goodness-of-fit tests. In *Proceedings of the 33rd International Conference on Machine Learning (ICML)*, volume 48 of *Proceedings of Machine Learning Research*, pages 276–284. PMLR, 2016.
- [23] Krzysztof Chwialkowski, Heiko Strathmann, and Arthur Gretton. A kernel test of goodness of fit. In *Proceedings of the 33rd International Conference on Machine Learning (ICML)*, volume 48 of *Proceedings of Machine Learning Research*, pages 2606–2615. PMLR, 2016.
- [24] Anna Korba, Pierre-Cyril Aubin-Frankowski, Szymon Majewski, and Pierre Ablin. Kernel stein discrepancy descent. In *International Conference on Machine Learning (ICML)*, volume 139 of *Proceedings of Machine Learning Research*. PMLR, 2021.
- [25] Michael Arbel, Anna Korba, Adil Salim, and Arthur Gretton. Maximum mean discrepancy gradient flow. In *Advances in Neural Information Processing Systems (NeurIPS)*, 2019.
- [26] Berthy T. Feng, Jamie Smith, Michael Rubinstein, Huiwen Chang, Katherine L. Bouman, and William T. Freeman. Score-based diffusion models as principled priors for inverse imaging. In *Proceedings of the IEEE/CVF International Conference on Computer Vision (ICCV)*, 2023.
- [27] Alexandre Adam, Adam Coogan, Nikolay Malkin, Ronan Legin, Laurence Perreault-Levasseur, Yashar Hezaveh, and Yoshua Bengio. Posterior samples of source galaxies in strong gravitational lenses with score-based priors. *arXiv preprint arXiv:2211.03812*, 2022.
- [28] Ronan Legin, Alexandre Adam, Yashar Hezaveh, Laurence Perreault-Levasseur, D. Zhang, Francisco Villaescusa-Navarro, Shirley Ho, Siamak Ravanbakhsh, and Yoshua Bengio. Posterior sampling of the initial conditions of the universe from large-scale structure surveys with score-based generative models. *arXiv preprint arXiv:2304.03788*, 2023.
- [29] Bradley Efron. Tweedie’s formula and selection bias. *Journal of the American Statistical Association*, 106(496):1602–1614, 2011. doi: 10.1198/jasa.2011.111181.
- [30] Herbert E. Robbins. An empirical Bayes approach to statistics. In *Proceedings of the Third Berkeley Symposium on Mathematical Statistics and Probability*,

*Volume 1: Contributions to the Theory of Statistics*, pages 157–163. University of California Press, Berkeley, CA, 1956.

[31] Art B. Owen. *Monte Carlo: Theory, Methods and Examples*. Stanford University, 2013. URL <https://artowen.su.domains/mc/>. Online book.

[32] Christian P. Robert and George Casella. *Monte Carlo Statistical Methods*. Springer, New York, 2 edition, 2004. ISBN 978-0387212395.

[33] Étienne Pardoux. *Markov Processes and Applications: Algorithms, Networks, Genome and Finance*. John Wiley & Sons, Chichester, UK, 2008. ISBN 978-0-470-74556-9.

[34] Michael P. Allen and Dominic J. Tildesley. *Computer Simulation of Liquids*. Oxford University Press, 2 edition, 2017. ISBN 978-0198803201.

[35] Daan Frenkel and Berend Smit. *Understanding Molecular Simulation: From Algorithms to Applications*. Academic Press, 2 edition, 2001. ISBN 978-0122673511.

[36] Tan Bui-Thanh and Mark Andrew Girolami. Solving large-scale PDE-constrained Bayesian inverse problems with Riemann manifold Hamiltonian Monte Carlo. *Inverse Problems*, Special Issue:114014, 2014. <http://users.ices.utexas.edu/%7Etanbui/PublishedPapers/RMHMC.pdf>.

[37] Shiwei Lan, Tan Bui-Thanh, Mike Christie, and Mark Girolami. Emulation of higher-order tensors in manifold monte carlo methods for bayesian inverse problems. *Journal of Computational Physics*, 308:81 – 101, 2016. ISSN 0021-9991. doi: <https://doi.org/10.1016/j.jcp.2015.12.032>. URL <http://www.sciencedirect.com/science/article/pii/S0021999115008517>.

[38] Tan Bui-Thanh and Quoc P. Nguyen. FEM-based discretization-invariant mcmc methods for pde-constrained bayesian inverse problems. *Inverse Problems and Imaging*, 10(4):943–975, 2016. ISSN 1930-8337. doi: 10.3934/ipi.2016028. URL <http://aimsciences.org/journals/displayArticlesnew.jsp?paperID=13201>. <http://users.ices.utexas.edu/%7Etanbui/PublishedPapers/FEMBayesian.pdf>.

[39] Tan Bui-Thanh and Omar Ghattas. Analysis of the Hessian for inverse scattering problems. Part I: Inverse shape scattering of acoustic waves. *Inverse Problems*, 28(5):055001, 2012. doi: 10.1088/0266-5611/28/5/055001. <http://users.ices.utexas.edu/%7Etanbui/PublishedPapers/CompactI.pdf>.

[40] Tan Bui-Thanh and Omar Ghattas. Analysis of the Hessian for inverse scattering problems. Part II: Inverse medium scattering of acoustic waves. *Inverse Problems*, 28(5):055002, 2012. doi: 10.1088/0266-5611/28/5/055002. <http://users.ices.utexas.edu/%7Etanbui/PublishedPapers/CompactII.pdf>.

[41] Tan Bui-Thanh and Omar Ghattas. Analysis of the Hessian for inverse scattering problems. Part III: Inverse medium scattering of electromagnetic waves. *Inverse Problems and Imaging*, 2013. <http://users.ices.utexas.edu/%7Etanbui/PublishedPapers/EM3Dmedium.pdf>.

[42] Tan Bui-Thanh, Omar Ghattas, James Martin, and Georg Stadler. A computational framework for infinite-dimensional Bayesian inverse problems Part I: The linearized case, with application to global seismic inversion. *SIAM Journal on Scientific Computing*, 35(6):A2494–A2523, 2013. doi: 10.1137/12089586X. <http://users.ices.utexas.edu/%7Etanbui/PublishedPapers/InfiniteBayesianSisc13.pdf>.

[43] Tan Bui-Thanh, Carsten Burstedde, Omar Ghattas, James Martin, Georg Stadler, and Lucas C. Wilcox. Extreme-scale UQ for Bayesian inverse problems governed by PDEs. In *SC12: Proceedings of the International Conference for High Performance Computing, Networking, Storage and Analysis*, 2012. Gordon Bell Prize finalist, <http://users.ices.utexas.edu/%7Etanbui/PublishedPapers/sc12.pdf>.

- [44] Tan Bui-Thanh and Omar Ghattas. A scalable MAP solver for Bayesian inverse problems with Besov priors. *Inverse Problems and Imaging*, 9(1):27–53, 2015. <http://users.ices.utexas.edu/%7Etanbui/PublishedPapers/BesovMAP.pdf>.
- [45] Aad W. van der Vaart. *Asymptotic Statistics*. Cambridge University Press, 1998.
- [46] Augustine Kong, Jun S. Liu, and Wing Hung Wong. Sequential imputations and bayesian missing data problems. *Journal of the American Statistical Association*, 89(425):278–288, 1994.
- [47] Art B Owen. *Monte Carlo theory, methods and examples*. Stanford, 2013.
- [48] Jun S. Liu. Combined monte carlo strategies. *Handbook of Monte Carlo Methods*, pages 163–182, 2001.
- [49] Bernard W Silverman. *Density Estimation for Statistics and Data Analysis*. CRC press, 1986.
- [50] YP Mack and Murray Rosenblatt. Multivariate k-nearest neighbor density estimates. *Journal of Multivariate Analysis*, 9(1):1–15, 1979.
- [51] Larry Wasserman. *All of Nonparametric Statistics*. Springer, 2006.
- [52] Andrew M. Stuart. Inverse problems: A Bayesian perspective. *Acta Numerica*, 19:451–559, 2010. doi: doi:10.1017/S0962492910000061.
- [53] Jari Kaipio and Erkki Somersalo. *Statistical and Computational Inverse Problems*, volume 160 of *Applied Mathematical Sciences*. Springer-Verlag, New York, 2005.
- [54] H. J. Brascamp and E. H. Lieb. On extensions of the Brunn–Minkowski and Prékopa–Leindler theorems, including inequalities for log concave functions, and with an application to the diffusion equation. *Journal of Functional Analysis*, 22(4):366–389, 1976.
- [55] H. J. Brascamp and E. H. Lieb. Some inequalities for Gaussian measures and the long-range order of the one-dimensional plasma. In A. M. Arthurs, editor, *Functional Integration and its Applications*, pages 1–14. Clarendon Press, Oxford, 1975. Lecture at the Conference on Functional Integration, Cumberland Lodge, England.
- [56] Dominique Bakry and Michel Émery. Diffusions hypercontractives. In *Séminaire de Probabilités XIX 1983/84*, Lecture Notes in Mathematics, pages 177–206. Springer, 1985.
- [57] Michel Ledoux. *The Concentration of Measure Phenomenon*. American Mathematical Society, 2001.
- [58] Roman Vershynin. *High-Dimensional Probability*. Cambridge University Press, 2018.
- [59] Martin J. Wainwright. *High-Dimensional Statistics*. Cambridge University Press, 2019.